ORIGINAL PAPER

Spontaneous emergence of deformation bands in single-crystal plasticity simulations at small strain

M. Ryś[1,2] · **M. Kursa[1]** · **H. Petryk[1]**

Abstract

In metal single crystals, the observed formation of deformation banding pattern has been explained by greater latent hardening of slip systems than their self-hardening, which promotes spatial segregation of plastic slips and lamination towards single-slip domains. Numerical studies focusing on the formation of deformation bands usually involved initial imperfections, boundary-induced heterogeneity, or the postulate of minimal global energy expenditure which additionally promoted non-uniformity of deformation. This article analyses the case when no such mechanism enforcing locally non-uniform deformation is implemented in the finite element (FE) method, while the global system of equations of incremental equilibrium is solved in a standard way. The new finding in this paper is that the deformation banding pattern can appear spontaneously in FE simulations of homogeneous single crystals even in the absence of any mechanism favouring deformation banding in the numerical code. This has been demonstrated in several examples in the small strain formalism using a plane-strain model in which the twelve fcc slip systems are reduced to three effective plastic slip mechanisms. Incremental slips are determined at the Gauss-point level either by incremental work minimization in the rate-independent case or by rate-dependent regularization. In the rate-independent approach, the trust-region algorithm is developed for the selection of active slip systems with the help of the augmented Lagrangian method. Conditions under which a banding pattern appears spontaneously or is suppressed are discussed. In particular, a critical rate sensitivity exponent is identified.

Keywords Crystal plasticity · Small strain · Slip-system selection · Path instability · Microstructure formation · Finite element method

1 Introduction

This paper is concerned with spontaneous formation of deformation bands which, unlike the more frequently analysed separate shear bands, cover the entire volume of a plastically deformed metal single crystal. This phenomenon is well documented experimentally using various techniques [5–7, 12, 21, 27–29, 32, 56, 91, 95] and even considered 'a potentially most valuable tool for the understanding of the mechanism of plastic deformation' [46]. The phenomenon was explained [7, 8, 15, 53, 54] as the result of greater latent hardening of the slip systems than their self-hardening, which makes plastic flow easier when split into two families of deformation bands with alternating sets of active slip systems.

In models of such laminates, calculations based on energetic preference of a band pattern relative to uniform deformation of a single crystal were performed by assuming band formation in advance, e.g. [14, 15, 17, 23, 26, 36, 38, 43–45, 63, 67, 68, 75]. The consistency of energy minimization with the originally assumed incremental constitutive law requires the existence of an incremental potential, at least in the limit passage to the imagined exact solution, which is a general feature of the incremental energy minimization method [74]. Then the same method can be used to determine the set of active slip systems and incremental slips in each band as part of determining the response of a rate-independent laminate model.

✉ H. Petryk
hpetryk@ippt.pan.pl

M. Ryś
mrys@ippt.pan.pl

M. Kursa
mkursa@ippt.pan.pl

1 Institute of Fundamental Technological Research, Polish Academy of Sciences, Pawińskiego 5B, 02-106 Warsaw, Poland

2 NOMATEN Centre of Excellence, National Centre for Nuclear Research, Sołtana 7, 05-400 Otwock, Poland

Full field simulations that showed a deformation band pattern without assuming its existence a priori were rarer. In the rate-independent framework, such calculations using finite element (FE) method were first performed by global incremental energy minimization applied to polycrystal models with the vertex effect [78–80], but for single crystals predominantly used was the rate dependent (RD) regularization of the slip-system activity rule. In a convenient power-law approach to rate sensitivity applicable to creep [33], all slip-systems subjected to non-zero driving force are active and the slip-rates in a given state are uniquely defined [1, 18, 52, 70, 83], thus avoiding the need for their selection, as opposed to the rate-independent model. For a sufficiently small positive rate-sensitivity exponent, m, only plastic flow on slip systems subjected to a resolved shear stress close enough to a threshold value is relevant.

In field simulations of rate-dependent plasticity in single crystals, frequently no clear pattern of deformation bands emerged or separate localization bands appeared, e.g., [13, 34, 48, 49, 58, 59, 62, 86, 96]. If patterns with multiple narrow bands were found in RD simulations, they were typically triggered by suitable imperfections or boundary-induced heterogeneity [4, 24, 30, 35, 39, 61, 91, 93, 94], supported also by minimization of a non-convex incremental energy [22, 37, 47, 51, 92, 97]. We do not distinguish here the models involving slip gradients from the local models as they can give qualitatively similar results [93]. In this work, conventional crystal plasticity in its possibly simple form is isolated for study so as not to blur the main message.

The main goal of this work is to demonstrate that deformation banding can appear spontaneously in finite element simulations of homogeneous single crystals with strain hardening, even in the absence of any direct mechanism of favouring deformation banding. This poses a challenge, not yet fully explored in the literature, for robust numerical simulations of single-crystal plasticity in which the physically observed deformation band patterning would not be artificially suppressed but also not uncontrolled. In contrast to the widely studied formation of a single shear band triggered by material softening which requires appropriate regularization, cf. the recent examples [81, 85], the mesh-dependence of the width of individual deformation bands is not so crucial here. It is the orientation, slip-system activity, and volume fraction of the bands, rather than their width, that describe the overall features of the crystal deformation, which can only slightly depend on mesh density. This feature is inherently related to the yield-vertex effect, either sharp for conventional rate-independent models or rounded off by rate sensitivity or regularization. While this feature is theoretically clear for homogenized infinite laminates, FE simulations showing macroscopic mesh-independence of the results at variable detail resolution are rare, e.g. [79, 80].

In the rate-independent case, the key issue to be addressed is the selection of active slip systems at the material point level. A recent overview of existing algorithmic approaches to rate-independent crystal-plasticity can be found in [65, 77, 82, 87, 98], where further references are provided. The problem arises when more than five slip systems (or less in 2D problems) can be active simultaneously at a given point, so the set of active slip systems is not uniquely defined in advance and an additional selection criterion is needed. The small-strain analysis performed in this paper is limited to the symmetric slip-system interaction matrix that defines a linear relationship between slip rates and yield function rates. If this matrix is symmetric, and only if its submatrix for active slip systems is symmetric, the incremental energy minimization can be used as a well-founded criterion for selecting the slip-system set and determining the rate-independent incremental response at the material point [75, 76], see Sect. 3.

In this paper, the algorithmic difficulty related to nonunique selection of active slip-systems in the rate-independent modelling is overcome by the incremental work minimization at each Gauss point, without appealing to any lamination. A trust region algorithm [16] is developed for incremental energy minimization to address non-convexity of the minimized function of incremental slips and is presented in Sect. 4. It is combined with the augmented Lagrangian method [9] to address unilateral constraints for slip increments and implemented in an implicit backward-Euler computational scheme. An essential feature of the present algorithm is that, for a given strain increment, it provides incremental slips on previously unknown systems that converge to exact slip rates as the strain increment tends to zero. This algorithmic feature is ensured by minimizing an incremental energy expression up to the second-order terms with the explicit use of the constitutive matrix of interaction between slip-systems [76].

The rate-dependent constitutive algorithm is based on the standard equations [31, 70] and uses a fully implicit scheme. Its performance was found to be satisfactory; there are other algorithms being recently in use [20, 60].

The aforementioned two constitutive approaches are used here in FE simulations to demonstrate the possibility of obtaining a deformation band pattern without imposing any imperfection or any global minimization of incremental energy. Interestingly, this concerns also RD simulations, provided the rate sensitivity is sufficiently low to mimic the vertex effect in crystal plasticity. This is a difference from all the FE simulations reviewed above. Strongly nonuniform deformation under conditions that could give rise to perfectly uniform strain can be interpreted as a symptom of (physical or numerical) instability of the uniform deformation path [19, 71].

Several examples were case studied from various aspects to substantiate the qualitative conclusions regarding defor-

mation banding, obtained within the standard crystal plasticity framework with a latent-to-self hardening ratio greater than one. For the demonstration purposes and easier interpretation, the attention is limited here to the 2D model of plane strain, which was obtained [84] from the 3D fcc model by reducing the number of effective slip systems from twelve to three. The 2D model was later successfully used in a number of other works, e.g. [50, 55, 57, 93]. The 2D model is described in Sect. 5, and detailed comparison of the deformation band patterns obtained for the rate-independent and rate-dependent models is presented in Sect. 6. Extension to finite deformation and size effects is not included here.

2 The constitutive framework at small strain

The constitutive equations of conventional crystal plasticity in the geometrically linear setting are well known and are briefly quoted below only for the sake of completeness. The symmetric part of the displacement gradient ∇u is additively decomposed into two symmetric tensors,

$$(\nabla u)_{\text{sym}} = \varepsilon^{\text{e}} + \varepsilon^{\text{p}}, \tag{1}$$

where ε^{e} is the elastic strain tensor and ε^{p} is the traceless plastic strain tensor, $\text{tr}\varepsilon^{\text{p}} = 0$. The forward rate $\dot{\varepsilon}^{\text{p}}$ of ε^{p} reads

$$\dot{\varepsilon}^{\text{p}} = \sum_{\alpha} \dot{\gamma}^{\alpha} \mathbf{p}^{\alpha}, \quad \mathbf{p}^{\alpha} = (\mathbf{s}^{\alpha} \otimes \mathbf{m}^{\alpha})_{\text{sym}},$$
$$\mathbf{s}^{\alpha} \cdot \mathbf{m}^{\alpha} = 0, \quad \alpha \in \mathcal{N} = \{1, \dots, N\}, \tag{2}$$

where N denotes the number of slip systems, $\mathbf{p}^{\alpha}$ is defined as the symmetrized tensor product of two given orthogonal unit vectors, slip direction $\mathbf{s}^{\alpha}$ and slip-plane normal $\mathbf{m}^{\alpha}$, and $\dot{\gamma}^{\alpha}$ is the rate of plastic shear (called slip-rate) on the α-th slip system. The effect of crystallographic lattice rotation is neglected. The resolved shear stress τ^{α} on the α-th slip system is defined by

$$\tau^{\alpha} = \mathbf{s}^{\alpha} \cdot \boldsymbol{\sigma} \mathbf{m}^{\alpha} = \boldsymbol{\sigma} \cdot \mathbf{p}^{\alpha}, \tag{3}$$

where $\boldsymbol{\sigma}$ is the symmetric Cauchy stress tensor. It is determined from the elastic constitutive law

$$\boldsymbol{\sigma} = \frac{\partial \psi^{\text{e}}}{\partial \varepsilon^{\text{e}}} = \mathbb{C}^{\text{e}} \cdot \varepsilon^{\text{e}}, \quad \psi^{\text{e}}(\varepsilon^{\text{e}}) = \frac{1}{2}\varepsilon^{\text{e}} \cdot \mathbb{C}^{\text{e}} \cdot \varepsilon^{\text{e}}, \tag{4}$$

where $\mathbb{C}^{\text{e}}$ is the constant fourth-order elastic stiffness tensor of both minor and major symmetries. Throughout this paper, direct juxtaposition of two tensors means simple contraction and a central dot the full contraction.

The current critical value of τ^{α} is denoted by $\tau_{\text{cr}}^{\alpha} > 0$ and determined by time integration of the conventional strain-hardening law

$$\dot{\tau}_{\text{cr}}^{\alpha} = \sum_{\beta} h^{\alpha\beta} \dot{\gamma}^{\beta}, \qquad \alpha, \beta \in \mathcal{N}. \tag{5}$$

Hardening moduli $h^{\alpha\beta}$ are state-dependent parameters that describe self-hardening of slip systems (for $\alpha = \beta$) and cross-hardening due to slip-systems interactions (for $\alpha \neq \beta$, called latent hardening if $\dot{\gamma}^{\alpha} = 0 \neq \dot{\gamma}^{\beta}$).

The yield function is postulated in the usual form as

$$f^{\alpha} = \tau^{\alpha} - \tau_{\text{cr}}^{\alpha}, \qquad \alpha \in \mathcal{N}. \tag{6}$$

Taking time derivative of $\boldsymbol{\sigma}$ and f^{α}, after simple rearrangements the following constitutive rate-equations are obtained as a small-strain version of the equations established by Hill and Rice [25]:

$$\dot{\boldsymbol{\sigma}} = \mathbb{C}^{\text{e}} \cdot \dot{\varepsilon} - \sum_{\beta} \mathbb{C}^{\text{e}} \cdot \mathbf{p}^{\beta} \dot{\gamma}^{\beta},$$
$$\dot{f}^{\alpha} = \mathbf{p}^{\alpha} \cdot \mathbb{C}^{\text{e}} \cdot \dot{\varepsilon} - \sum_{\beta} g^{\alpha\beta} \dot{\gamma}^{\beta}, \quad \alpha, \beta \in \mathcal{N}. \tag{7}$$

The slip-systems interaction matrix, $(g^{\alpha\beta})$, is related to the hardening moduli matrix, $(h^{\alpha\beta})$, by

$$g^{\alpha\beta} = h^{\alpha\beta} + \mathbf{p}^{\alpha} \cdot \mathbb{C}^{\text{e}} \cdot \mathbf{p}^{\beta}. \tag{8}$$

Note that $(g^{\alpha\beta}) = (g^{\beta\alpha})$ if the hardening moduli matrix is symmetric, $(h^{\alpha\beta}) = (h^{\beta\alpha})$. This is in contrast to the finite deformation theory (cf. [25, 69, 75]) where an additional, generally non-symmetric term enters $(g^{\alpha\beta})$ due to geometric interaction between slip systems.

The rate-independent rule of slip-systems activity reads

$$\dot{\gamma}^{\alpha} \geq 0, \quad f^{\alpha} \leq 0, \quad f^{\alpha} \dot{\gamma}^{\alpha} = 0$$
$$(\text{no sum}) \quad \forall \alpha \in \mathcal{N}. \tag{9}$$

Note that pairs $(\mathbf{s}^{\alpha}, \mathbf{m}^{\alpha})$ and $(-\mathbf{s}^{\alpha}, \mathbf{m}^{\alpha})$ are understood here as defining different slip systems, whose number is therefore doubled (2×12 in fcc case). Importantly, to determine slip rates $\dot{\gamma}^{\alpha}$ in a given state, the consistency conditions must be used,

$$\dot{f}^{\alpha} \leq 0, \quad \dot{f}^{\alpha} \dot{\gamma}^{\alpha} = 0 \quad (\text{no sum}) \quad \text{if } f^{\alpha} = 0, \tag{10}$$

where $\dot{f}^{\alpha}$ is found from Eq. (7)$_2$. In general, this is still insufficient to determine all slip rates $\dot{\gamma}^{\alpha}$ uniquely if $f^{\alpha} = 0$ for linearly dependent slip systems. To overcome this difficulty, especially when matrix $(h^{\alpha\beta})$ is indefinite due to

cross-hardening stronger than self-hardening, we will consider two different approaches at a material point level: incremental energy minimization [67, 68, 72, 74] (as reference here) and the rate-dependent regularization (as the most commonly used).

3 Incremental energy minimization

3.1 The virtual work rate

The rate of free energy density function $\psi(\boldsymbol{\varepsilon}^{\mathrm{e}}, \boldsymbol{\xi})$, dependent on elastic strain $\boldsymbol{\varepsilon}^{\mathrm{e}}$ and internal variables $\boldsymbol{\xi}$ at fixed temperature and taken per unit volume, reads

$$\dot{\psi} = \boldsymbol{\sigma} \cdot \dot{\boldsymbol{\varepsilon}}^{\mathrm{e}} + \frac{\partial \psi}{\partial \boldsymbol{\xi}} \cdot \dot{\boldsymbol{\xi}}. \tag{11}$$

Assuming that $(\partial \psi / \partial \boldsymbol{\xi}) \cdot \dot{\boldsymbol{\xi}} = \sum_\alpha p^\alpha \dot{\gamma}^\alpha$, where p^α are state-dependent parameters related to hardening, the expression for $\dot{\psi}$ is rearranged straightforwardly as follows

$$\dot{\psi} = \boldsymbol{\sigma} \cdot \dot{\boldsymbol{\varepsilon}} - \sum_\alpha \chi^\alpha \dot{\gamma}^\alpha, \qquad \chi^\alpha = \tau^\alpha - p^\alpha. \tag{12}$$

In the following we tacitly assume that α, β run through the set $\mathcal{N}$.

The rate-independent dissipation function that expresses the virtual dissipation rate per unit volume is defined by

$$\begin{aligned} D &= \sum_\alpha \chi_{\mathrm{cr}}^\alpha \dot{\gamma}^\alpha \geq 0, \\ \chi_{\mathrm{cr}}^\alpha &= \tau_{\mathrm{cr}}^\alpha - p^\alpha \geq 0, \qquad \dot{\gamma}^\alpha \geq 0. \end{aligned} \tag{13}$$

The total *virtual* work-rate per unit volume now reads

$$\begin{aligned} \dot{w} &= \dot{\psi} + D \\ &= \boldsymbol{\sigma} \cdot \dot{\boldsymbol{\varepsilon}} - \sum_\alpha f^\alpha \dot{\gamma}^\alpha, \\ f^\alpha &= \chi^\alpha - \chi_{\mathrm{cr}}^\alpha = \tau^\alpha - \tau_{\mathrm{cr}}^\alpha, \end{aligned} \tag{14}$$

which includes the power of perturbing forces that compensate a possible gap between χ^α and $\chi_{\mathrm{cr}}^\alpha$. It follows that the slip-system activity rule (9) admits the *equivalent* variational formulation [75]:

$$\dot{w} \rightarrow \min_{\dot{\gamma}^\alpha \geq 0} \quad \text{for given } \dot{\boldsymbol{\varepsilon}}. \tag{15}$$

This constitutes the basis for the incremental energy minimization which, however, requires an additional symmetry assumption $(g^{\alpha\beta}) = (g^{\beta\alpha})$.

3.2 The incremental energy minimization in implicit time-integration scheme

The work-rate expression (14) is now integrated with respect to time $t \in [t_n, t_{n+1}]$ under the additional assumption that the slip-system interaction matrix in the constitutive rate equation $(7)_2$ is symmetric,

$$(g^{\alpha\beta}) = (g^{\beta\alpha}) \quad \Longleftrightarrow \quad (h^{\alpha\beta}) = (h^{\beta\alpha}) \tag{16}$$
for diagonally symmetric $\mathbb{C}^{\mathrm{e}}$.

As already remarked, the above equivalence holds true only in the small-strain format where the relative spin of the material and lattice is neglected.

Denote by prefix Δ an increment of any quantity ϕ in the time interval $[t_n, t_{n+1}]$ as $\Delta\phi = \phi_{n+1} - \phi_n$ for $\Delta t = t_{n+1} - t_n$. In the implicit time-integration scheme applied to the work-rate expression (14), we obtain to first order

$$\Delta_1 w = \boldsymbol{\sigma}_{n+1} \cdot \Delta\boldsymbol{\varepsilon} - \sum_\alpha f_{n+1}^\alpha \Delta\gamma^\alpha \tag{17}$$

and to second order

$$\Delta w = \frac{1}{2}(\boldsymbol{\sigma}_n + \boldsymbol{\sigma}_{n+1}) \cdot \Delta\boldsymbol{\varepsilon} - \frac{1}{2}\sum_\alpha (f_n^\alpha + f_{n+1}^\alpha)\Delta\gamma^\alpha. \tag{18}$$

Time integration of the constitutive rate equations (backward Euler for $\dot{f}^\alpha$) gives

$$\Delta\boldsymbol{\sigma} = \boldsymbol{\sigma}_{n+1} - \boldsymbol{\sigma}_n = \mathbb{C}^{\mathrm{e}} \cdot \Delta\boldsymbol{\varepsilon} - \sum_\alpha \mathbb{C}^{\mathrm{e}} \cdot \mathbf{p}^\alpha \Delta\gamma^\alpha, \tag{19}$$

$$\Delta f^\alpha = f_{n+1}^\alpha - f_n^\alpha = \mathbf{p}^\alpha \cdot \mathbb{C}^{\mathrm{e}} \cdot \Delta\boldsymbol{\varepsilon} - \sum_\beta g_{n+1}^{\alpha\beta} \Delta\gamma^\beta. \tag{20}$$

Combining the above equations, we obtain

$$\begin{aligned} \Delta w &= \boldsymbol{\sigma}_{n+1} \cdot \Delta\boldsymbol{\varepsilon} - \sum_\alpha f_{n+1}^\alpha \Delta\gamma^\alpha - \frac{1}{2}\Delta\boldsymbol{\varepsilon} \cdot \mathbb{C}^{\mathrm{e}} \cdot \Delta\boldsymbol{\varepsilon} \\ &\quad + \Delta\boldsymbol{\varepsilon} \cdot \sum_\alpha \mathbb{C}^{\mathrm{e}} \cdot \mathbf{p}^\alpha \Delta\gamma^\alpha - \frac{1}{2}\sum_{\alpha,\beta} \Delta\gamma^\alpha \, g_{n+1}^{\alpha\beta} \, \Delta\gamma^\beta. \end{aligned} \tag{21}$$

On using Eqs. (16), (19) and (20) for given f_n^α, it follows that the incremental energy function (21) acts as a constitutive potential for f_{n+1}^α at given $g_{n+1}^{\alpha\beta}$, viz.

$$f_{n+1}^\alpha = -\left.\frac{\partial \Delta w}{\partial \Delta\gamma^\alpha}\right|_{\Delta\boldsymbol{\varepsilon}} \quad \forall\alpha \in \mathcal{N}. \tag{22}$$

By incremental energy minimization applied to function (21), from the Kuhn–Tucker conditions necessary for a minimum we obtain

$$\Delta w \rightarrow \min_{\Delta \gamma^\alpha \geq 0} \quad \Longrightarrow$$
$$f_{n+1}^\alpha \leq 0 \quad \text{and} \quad f_{n+1}^\alpha \Delta \gamma^\alpha = 0 \quad \forall \alpha \in \mathcal{N} \tag{23}$$

as the time-discrete consistency conditions. The Hessian of function Δw with respect to $\Delta \gamma^\alpha$,

$$g_{n+1}^{\alpha\beta} = \left. \frac{\partial^2 \Delta w}{\partial \Delta \gamma^\alpha \partial \Delta \gamma^\beta} \right|_{\Delta \boldsymbol{\varepsilon}}, \tag{24}$$

may be indefinite for linearly dependent slip systems if matrix $(h^{\alpha\beta})$ is indefinite. The minimized function Δw is thus generally non-convex which requires appropriate numerical treatment.

For algorithmic purposes, the incremental work density (21) is rearranged as a quadratic energy function depending on $\Delta \gamma^\alpha$ for given $\Delta \boldsymbol{\varepsilon}$,

$$\Delta e(\Delta \gamma^\alpha) = - \sum_\alpha (f_n^\alpha + \Delta \boldsymbol{\varepsilon} \cdot \mathbb{C}^{\mathrm{e}} \cdot \mathbf{p}^\alpha) \Delta \gamma^\alpha$$
$$+ \frac{1}{2} \sum_{\alpha,\beta} \Delta \gamma^\alpha g_{n+1}^{\alpha\beta} \Delta \gamma^\beta + (\boldsymbol{\sigma}_n + \frac{1}{2} \mathbb{C}^{\mathrm{e}} \cdot \Delta \boldsymbol{\varepsilon}) \cdot \Delta \boldsymbol{\varepsilon}, \tag{25}$$

where $g_{n+1}^{\alpha\beta}$ are taken from the preceding sub-iteration within the time step $[t_n, t_{n+1}]$. In the current small-strain format, $\mathbb{C}^{\mathrm{e}}$ and $\mathbf{p}^\alpha$ are constant, $\Delta \boldsymbol{\varepsilon}$ is prescribed, and f_n^α and $\boldsymbol{\sigma}_n$ are known from the previous time step.

This is a simplified version of the more general approach developed by Petryk and Kursa [76] which applies to finite deformation. A non-trivial extension to a non-symmetric matrix $(g^{\alpha\beta})$ is given in [77]. For the purposes of the present finite element calculations, a minimization algorithm was developed which is described in the next section.

4 Algorithmic approach

The *Trust Region* method [16] is effectively used for the non-convex minimization problem, here for the augmented Langrangian based on function (25), where direct application of Newtons method can be hindered by an indefinite Hessian matrix. Central to the Trust Region approach is the formulation and solution of a subproblem at each iteration that aims to minimize a quadratic model of the objective function within a specified trust region. Crucially, when dealing with a non-positive definite Hessian – which can lead to indeterminate or directionally incorrect steps – the method requires modifying or 'regularizing' the Hessian within the subproblem to ensure that it gives a meaningful direction for progression. Therefore, the trust region not only restricts the step size to maintain model fidelity, but also dynamically adjusts the region boundaries based on the prediction accuracy of the previous step. This dual adaptation—both in step size

and in the handling of the Hessian's indefiniteness—supports the robustness and effectiveness of this method in navigating complex landscapes of non-convex problems.

The *Augmented Lagrangian* method [9, 66] is used in order to deal with inequality constraints imposed on incremental slips $\Delta \gamma^\alpha$, which transforms the local constrained minimization problem formulated in Sect. 3.2 to a smooth unconstrained minimization problem. The unconstrained search for a local minimum of the Lagrangian when it is strictly convex can be performed using the Newton method.

The *implicit backward-Euler* computational scheme is used throughout. In result, the algorithm enables automatic selection of the active slip systems during FE simulations, so that an energetically preferable solution at every Gauss point is found that satisfies the discrete consistency conditions (23) at the end of each time step within the required tolerance.

While the above three algorithmic approaches considered separately are well known, their combination in the rate-independent crystal plasticity algorithm applied to FE calculations appears to be new. Therefore, the algorithm is described in more detail below.

4.1 Trust region algorithm for augmented Lagrangian in rate-independent crystal plasticity

The purpose of the algorithm is to find a solution that satisfies the conditions in Eq. (23) by minimizing the incremental energy function, Eq. (25). By finding a solution we mean finding a set of active slip systems and incremental slips for this set of active slip systems. Since the increments of plastic slips in the rate-independent model used must be non-negative, $\Delta \gamma^\alpha \geq 0$, the optimization problem is of the constrained type. To ensure the $\Delta \gamma^\alpha \geq 0$ requirement is finally satisfied, the incremental energy (25) is augmented by additional functions φ^α of Lagrange multipliers and slip increments:

$$\varphi^\alpha = \begin{cases} \lambda^\alpha \Delta \gamma^\alpha + \frac{\mu}{2} (\Delta \gamma^\alpha)^2 & \text{if } \lambda^\alpha + \mu \Delta \gamma^\alpha < 0, \\ -\frac{1}{2\mu} (\lambda^\alpha)^2 & \text{otherwise,} \end{cases} \tag{26}$$

where λ^α denotes α-th Lagrange multiplier and μ a regularization parameter which need *not* tend to infinity to obtain an exact solution. Adding φ^α to Δe reduces the constrained minimization problem for Δe to a more convenient, unconstrained and smooth optimization problem for the resulting Lagrangian, defined as follows [76]:

$$\mathcal{L} = \Delta e + \varphi \rightarrow \min_{(\Delta \gamma^\alpha) \in \mathbb{R}^N} \quad \text{with } \varphi = \sum_\alpha \varphi^\alpha. \tag{27}$$

It should be noted that in our algorithm (Algorithm 1) the primal unknowns $\Delta \gamma^\alpha$ and Lagrange multipliers λ^α as well as

Algorithm 1 Trust region algorithm with Lagrange multipliers for constraints (after [64], with modifications)

Step 0: *Input*
1: *set* $\Delta\gamma^\alpha = 0, \quad \lambda^\alpha = 0$ ▷ initial incremental slips and Lagrange multipliers
2: *set* $\Delta, \quad \Delta_{\max}$ ▷ initial and maximal radius of trust region
3: *set* $\mu, \quad \eta = 1/\mu^{0.1}, \quad \text{tol1} = 10^{-16}$ ▷ initial regularization parameters and tolerance
4: *define* $\hat{\mathcal{L}} = \mathcal{L}(\Delta\gamma^\alpha)|_{\lambda^\alpha,\eta} \quad \hat{G} = \nabla\mathcal{L}(\Delta\gamma^\alpha)|_{\lambda^\alpha,\eta} \quad \hat{B} = \nabla\nabla\mathcal{L}(\Delta\gamma^\alpha)|_{\lambda^\alpha,\eta}$
Step 1:
5: *insert* $(\Delta, \hat{G}, \hat{B})$ *into the subproblem in Algorithm* 2 *and return approximate solution* $\delta\Delta\gamma^\alpha$ *to problem* (29)
6: *set* $\Delta\gamma^\alpha_{\text{trial}} = \Delta\gamma^\alpha + \delta\Delta\gamma^\alpha$
Step 2:
7: *compute* $\hat{\mathcal{L}}_{\text{trial}} = \mathcal{L}(\Delta\gamma^\alpha_{\text{trial}}, \lambda^\alpha, \mu)$ *and* $\rho = \frac{\hat{\mathcal{L}}_{\text{trial}} - \hat{\mathcal{L}}}{Q(\delta\Delta\gamma)}$
Step 3:
8: **if** $\rho \geq 0.25$ **then**
9: $\quad \Delta\gamma^\alpha \leftarrow \Delta\gamma^\alpha_{\text{trial}}$ ▷ accept trial solution
10: $\quad c^\alpha \leftarrow \min(0, \Delta\gamma^\alpha)$
11: $\quad$ **if** $|(c^\alpha)| \leq \eta$ **then**
12: $\quad\quad \mu \leftarrow \mu, \quad \eta \leftarrow \eta/\mu^{0.9}$
13: $\quad\quad \lambda^\alpha \leftarrow \min(0, \lambda^\alpha + \mu\,\Delta\gamma^\alpha)$ ▷ update Lagrange multipliers
14: $\quad$ **else**
15: $\quad\quad \mu \leftarrow 2\mu, \quad \eta \leftarrow 1/\mu^{0.1}$ ▷ increase regularization parameter
16: $\quad$ **end if**
17: $\quad \hat{\mathcal{L}}, \quad \hat{G}, \quad \hat{B}$ ▷ calculate new values of Lagrangian, gradient and Hessian
18: **end if**
Step 4: ▷ decide whether to update the radius value
19: **if** $\rho \leq 0.3$ **then**
20: $\quad \Delta \leftarrow \Delta/4$
21: **end if**
22: **if** $\rho \geq 0.85$ **and** $|(\Delta\gamma^\alpha)| = \Delta$ **then**
23: $\quad \Delta \leftarrow \min(2\Delta, \Delta_{\max})$
24: **end if**
Step 5:
25: **if** $|\hat{G}| \leq \text{tol1}$ **and** $|(c^\alpha)| \leq \text{tol1}$ **then**
26: $\quad$ **stop** and **return** solution $\Delta\gamma^\alpha$
27: **else**
28: $\quad$ **go to Step** 1.
29: **end if**
Output: $\Delta\gamma^\alpha$

regularization parameter μ are updated iteratively in a manner described later. This differs from the alternative approach of using the augmented Lagrangian method for a convex objective function, where the problem is solved in a monolithic fashion for constant μ for both the primal unknowns and Lagrange multipliers.

In the present paper, the trust region method with an iterative optimization [89] is employed to find a minimum of a given objective function, $\mathcal{L}$. The trust region method was used for solving other plasticity problems with nonunique solutions, cf. [79, 80] and references therein. The core idea of a trust region method is to approximate the original Lagrangian $\mathcal{L}$ with a quadratic model Q constructed from a truncated Taylor series expansion with respect to $\Delta\gamma$ within a specific region around a particular point, for other parameters fixed, i.e.

$$\mathcal{L}(\Delta\gamma + \delta\Delta\gamma) \approx \mathcal{L}(\Delta\gamma) + Q(\delta\Delta\gamma)$$
$$\text{with } |\delta\Delta\gamma| \leq \Delta, \quad \text{where } \delta\Delta\gamma = (\delta\Delta\gamma^\alpha). \tag{28}$$

Hence, in the present case the problem boils down to minimizing, at each iteration, the quadratic model. Specifically:

$$\text{minimize } Q(\delta\Delta\gamma) = G^{\mathrm{T}}\delta\Delta\gamma + \frac{1}{2}\delta\Delta\gamma^{\mathrm{T}}B\delta\Delta\gamma$$
$$\text{subject to } |\delta\Delta\gamma| \leq \Delta, \tag{29}$$

where G is the gradient of $\mathcal{L}$ and B is the Hessian of $\mathcal{L}$ with respect to $\Delta\gamma^\alpha$. The parameter Δ denotes the value of the trust region radius that restricts the scope of the local search. Within this trust region, including its boundary, the quadratic model is minimized iteratively by adjusting the region's size and fine-tuning the approximation to ultimately converge to a solution that minimizes the original objective function.

In order to solve the above subproblem (29) a modified version of algorithm proposed by Moré and Sorensen [64] was implemented (Algorithm 2). In the current version of the algorithm, a direct calculation of the lowest eigenvalue and corresponding eigenvector is employed when needed, representing the primary modification from the original algorithm,

---

Algorithm 2 Subproblem solution (after [64], with modification, cf. [16, Alg. 7.3.6])

Step 0: *Input*
1: *set* Δ, $\hat{G}$, $\hat{B}$ ▷ Radius, Gradient, Hessian
2: *set* tol2 $= 10^{-4}$, $\epsilon = 10^{-5}$ ▷ Algorithmic parameters: tolerance, small positive number
Step 1:
3: **if** $\hat{B}$ *is positive definite* **then**
4:     $\lambda \leftarrow 0$ *and solve* $\hat{B}s = -\hat{G}$
5:     **go to Step** 3
6: **else**
7:     *compute the lowest eigenvalue* λ_1 *of* $\hat{B}$ *and set* $\lambda \leftarrow -\lambda_1$
8: **end if**
Step 2:
9: *set* $\hat{B} \leftarrow \hat{B} + (\lambda + \epsilon)\,I$ *and make Cholesky factorization* $\hat{B} = LL^T$ *and solve* $LL^Ts = -\hat{G}$
Step 3:
10: **if** $|s| \leq \Delta$ **then**
11:     **if** $\lambda = 0$ **or** $|s| = \Delta$ **then**
12:         **return** s
13:     **else**   ▷ Hard case
14:         *compute an eigenvector* u_1 *corresponding to* λ_1
15:         *find the root* α *of the equation* $|s + \alpha u_1| = \Delta$
16:         *set* $s \leftarrow s + \alpha u_1$ *and* **return** s
17:     **end if**
18: **else**
Step 4:
19:     **repeat**
20:         *solve* $Lw = s$
21:         *compute* $\lambda \leftarrow \lambda + \left(\frac{|s|-\Delta}{\Delta}\right)\left(\frac{|s|^2}{|w|^2}\right)$
22:         *set* $\hat{B} \leftarrow \hat{B} + \lambda\,I$ *and make Cholesky factorization* $\hat{B} = LL^T$
23:         *solve* $LL^Ts = -\hat{G}$
24:     **until** $||s| - \Delta| \leq$ tol2 Δ
25:     **return** s
26: **end if**
Output: $\delta\Delta\gamma \leftarrow s$

---

which relied on proper estimates of these quantities (cf. [16]). If the Hessian is not positive definite and since the number of unknowns is relatively small, it is modified by finding the smallest eigenvalue λ_1 (see Algorithm 2, step 1). The smallest eigenvalue, say λ_1, is computed with the use of LAPACK library [3] integrated in the AceGen system [41]. If $\lambda_1 \leq 0$ then Hessian B is modified to $B + (\epsilon - \lambda_1)I$, where I is the identity matrix and $0 < \epsilon \ll 1$. For further details and other possibilities of Hessian modification, the reader is referred to [66, Chapter 3].

The modification of a singular Hessian in the rate-independent crystal plasticity is similar in spirit to the perturbation technique proposed in [62, (Sec. 4.1.3)], while the singular value decomposition, cf. [2], is not used here. The essential difference between those approaches and the present work is that here the set of active slip systems is not assumed in advance when determining slip increments by incremental energy minimization.

The algorithm described in Algorithm 2, which is used to solve the subproblem, is included in the trust region algorithm, Algorithm 1 step 1. Of particular significance, in the trust region algorithm, is the assessment of whether the reduction in the objective function, accomplished through this local minimization, is consistent with the anticipated reduction predicted by the quadratic model. This measure of algorithm performance is denoted by ρ, see Algorithm 1 step 2. When the approximation meets the stipulated criteria of accuracy, the solution is accepted, and the algorithm proceeds to the subsequent iteration (Algorithm 1 step 3). If not, an adjustment of the trust region radius is made (Algorithm 1 step 4).

In addition to the standard trust region method, the step in which the approximation is deemed satisfactory and the solution is accepted also involves updating the Lagrange multipliers or regularization parameter (Algorithm 1 step 3). Importantly, either Lagrange multipliers or the regularization parameter are updated, but not both at the same time. The decision of which one must be updated is made based on the constraint violation functions denoted as c^α in Algorithm 1 step 3, cf. [66, Alg. 17.4]. The Lagrange multipliers are updated according to:

$$\lambda^\alpha \leftarrow \min(0, \lambda^\alpha + \mu\,\Delta\gamma^\alpha). \tag{30}$$

A more detailed description of the augmented Lagrangian method can be found in [9] and [66, Chapter 17].

In computational algorithms, the fine-tuning of parameters to the specifics of the problem under investigation is

crucial for optimizing both performance and accuracy. The constants like 0.1, 0.9, 2, 0.3, and 0.85, utilized within the described algorithm, while initially chosen based on conventional practices, possess a degree of flexibility. Altering these values allows for the adaptation of the algorithm to various problems, without compromising its theoretical convergence properties. In our analysis, we observed improvements in both the robustness and performance of the algorithm by commencing with a low regularization parameter μ (e.g., values such as 10 or 5) and adopting a modest increase strategy—doubling the value if needed.

To speed up the whole procedure at the Gauss point level, the Newton method was first used for the reduced set of equations based on the previously found set of active slip systems (if available from the previous step). Such approach is justified since the change of active slip systems does not happen too frequently [76]. Importantly, such modification does not influence the final solution but speeds up the calculations. Moreover, after obtaining a solution through the trust region algorithm, the Newton method was used for the reduced set of equations for two reasons: first to obtain high precision of the solution in the fully implicit scheme (this is helpful especially when e.g. $g^{\alpha\beta}$ is a nonlinear function of actual values of γ^α), and second to obtain an element tangent matrix through the automatic differentiation available in AceGen. The whole procedure allowed for meeting consistency conditions with precision $f^\alpha \leq 10^{-8}$ and $|f^\alpha \Delta\gamma^\alpha| \leq 10^{-8}$ at the end of each computational time step.

The general algorithm described above has been incorporated into the finite element method (FEM). The implementation has been done with the use of the AceGen code generator which combines the symbolic capabilities of Mathematica and an automatic differentiation (AD) technique. AceGen along with the AceFEM module provide a convenient system for generating numerical procedures and computing particular problems in FEM [41, 42]. In the present study, the minimization problem has been tackled locally, necessitating the invocation of the trust region procedure at each Gauss point to determine a solution $\Delta\gamma^\alpha$ for given $\Delta\boldsymbol{\varepsilon}$. Consequently, akin to conventional FEM codes, the global unknowns are restricted solely to displacements. The global level employs a Newton scheme, with FE simulations conducted using an adaptive deformation step. Displacements are interpolated using standard biquadratic shape functions, specifically 9-node quadrilaterals in a two-dimensional finite element setting. Full integration scheme with (3×3) Gauss quadrature points was used. Despite the higher computational costs of the biquadratic element, it was used to avoid effects such as hourglass or shear locking phenomena that may occur in lower order elements. All computations were executed on a desktop PC featuring a single Intel Core i7-4790K 4.00GHz processor with 32GB RAM under the Windows operating system.

4.2 Notes on rate-dependent algorithm

As the algorithm for rate-independent crystal plasticity is later compared with rate-dependent one, some notes about the latter formulation are provided here. The rate-dependent version of crystal plasticity framework is usually used to circumvent the problem of non-uniqueness in the selection of active slip systems. The standard approach is to employ the following explicit equation for the plastic slip rate on each slip system [33, 70]

$$\dot{\gamma}^\alpha = \dot{\gamma}_0 \, \text{sign}(\tau^\alpha) \left(\frac{|\tau^\alpha|}{\tau_{\text{cr}}^\alpha} \right)^r, \quad r = 1/m, \quad m > 0, \qquad (31)$$

where the reference slip rate $\dot{\gamma}_0$ is a material parameter and will be assumed as constant for all slip-systems, and m is the strain-rate-sensitivity exponent which is treated here as a case study parameter. Importantly, in this formulation the plastic slip increments or rates $\dot{\gamma}^\alpha$ may be positive or negative, therefore the incremental hardening law (5) must be replaced with

$$\dot{\tau}_{\text{cr}}^\alpha = \sum_\beta h^{\alpha\beta} \, |\dot{\gamma}^\beta|. \qquad (32)$$

As it is known, when the exponent r is large, the coupled set of equations becomes highly non-linear, leading to slow convergence and requiring small steps. A common approach is to begin with a lower exponent value, obtain a solution, and then increase the exponent gradually. However, in our rate-dependent algorithm, we employ a different method that has been found to outperform the former approach. The idea is that at every first iteration, the plastic slip rates are found using an explicit step based on the rates from previous convergent step, cf. [31, 70], next the solution is used as a starting point in a fully implicit scheme. This algorithmic approach enabled calculations with a much higher exponent r than is typically encountered in the literature. For other algorithms which could be potentially used, see e.g. [20, 60].

5 2D plane-strain model

Under special circumstances, the 3D crystal plasticity model can be reduced, following [84], to a 2D plane-strain model. The detailed formulation can be found in [50] and [55], therefore only the basic formulae are repeated in the following. The deformation of an fcc single crystal within the crystallographic plane (110) is realized assuming an initial orientation of the crystallographic lattice with respect to a fixed reference frame (x_i), $i = 1, 2, 3$. The lattice is initially rotated in the (110) plane counter-clockwise by angle ω, as illustrated in Fig. 1. In the case of orientation $\omega = 0$ the reference frame
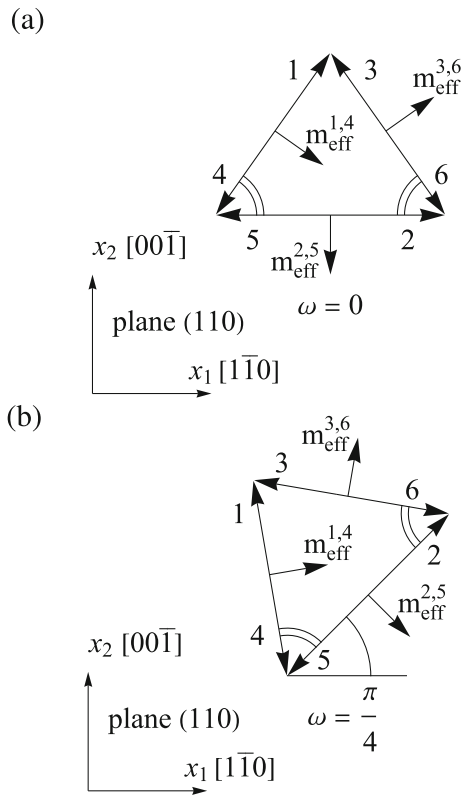
(a)

(b)

Fig. 1 2D in-plane effective slip-systems in case of orientation **a** $\omega = 0$ and **b** $\omega = \pi/4$. The slip-plane normals for effective slip-systems are denoted by $\mathbf{m}_{\text{eff}}^K$, while the corresponding slip directions, $\mathbf{s}_{\text{eff}}^K$, are only indicated by the numbers $K = 1, \ldots, 6$

is defined such that x_1 axis collinear with the $[1\bar{1}0]$ direction, x_2 axis with the $[00\bar{1}]$ direction, and the x_3 axis with $[110]$ direction, cf. Fig. 1a.

For the fcc crystal, out of the twelve positive and twelve negative crystallographic slip-systems of the 3D model, defined in Table 1 using the standard notation following [90], only part of the slip-systems can be activated. Considering both positive and negative, there are twelve slip-systems $(a3, b3, c1, c2, d1, d2, a\bar{3}, b\bar{3}, c\bar{1}, c\bar{2}, d\bar{1}, d\bar{2})$ that can be activated during deformation in (110) plane-strain conditions.

These twelve crystallographic slip-systems will flow in pairs. It is sufficient to consider six effective in-plane slip-systems, which are pairs of the crystallographic slip-systems. The positive effective slip-systems $(1, 2, 3)$ indexed by K consist of the following pairs $(d2 + d\bar{1}, a\bar{3} + b3, c\bar{2} + c1)$, respectively, as shown in Table 2. The negative effective slip-

systems (4, 5, 6) correspond to pairs $(d\bar{2}+d1, a3+b\bar{3}, c2+c\bar{1})$, respectively. In the rate-dependent description, in contrast to the rate-independent framework where $\Delta\gamma^\alpha \geq 0$ for all α, the negative effective slip-systems need not be considered separately.

The angle between the effective slip directions $\mathbf{s}_{\text{eff}}^{1,4}$ and $\mathbf{s}_{\text{eff}}^{2,5}$, as well as between the directions $\mathbf{s}_{\text{eff}}^{3,6}$ and $\mathbf{s}_{\text{eff}}^{2,5}$, cf. Fig. 1, is equal to $\arctan(\sqrt{2}) \approx 54.7°$.

The constitutive description of the 2D plane-strain model is summarized in terms of effective (in-plane) quantities, after [55], as follows. Plastic strain rate results from slips $\dot{\gamma}_{\text{eff}}^K$ on effective slip-systems indexed by K,

$$\dot{\boldsymbol{\varepsilon}}^{\text{p}} = \sum_K \dot{\gamma}_{\text{eff}}^K \mathbf{p}_{\text{eff}}^K, \quad \mathbf{p}_{\text{eff}}^K = \left(\mathbf{s}_{\text{eff}}^K \otimes \mathbf{m}_{\text{eff}}^K\right)_{\text{sym}},$$
$$K \in \mathcal{N}_{\text{eff}} = \{1, \ldots, 6\},$$

(33)

where a unit vector $\mathbf{s}_{\text{eff}}^K$ defines an effective slip direction and $\mathbf{m}_{\text{eff}}^K$ an effective slip plane normal, as shown in Table 2.

The effective yield function $f_{\text{eff}}^K = \tau_{\text{eff}}^K - \tau_{\text{cr-eff}}^K$ for the Kth individual slip-systems is defined as a difference of the effective resolved shear stress $\tau_{\text{eff}}^K = \boldsymbol{\sigma} \cdot \mathbf{p}_{\text{eff}}^K$ and its critical value $\tau_{\text{cr-eff}}^K$ that obeys the evolution rule

$$\dot{\tau}_{\text{cr-eff}}^K = \sum_L h_{\text{eff}}^{KL} \dot{\gamma}_{\text{eff}}^L, \qquad K, L \in \mathcal{N}_{\text{eff}}.$$

(34)

The hardening law for the effective critical resolved shear stresses (in terms of the effective in-plane slips) has been specified by Lewandowski and Stupkiewicz [55]. The initial value of critical shear stress $\tau_{\text{cr-eff}}^K$ at $\gamma_{\text{eff}}^K = 0$ is related to initial yield stress τ_0 by $\tau_{0\text{-eff}}^K = w^K \tau_0$, where w^K are the weights for effective slip-systems K,

$$(w^K) = \left(\frac{2}{\sqrt{3}} \ \sqrt{3} \ \frac{2}{\sqrt{3}} \ \frac{2}{\sqrt{3}} \ \sqrt{3} \ \frac{2}{\sqrt{3}}\right)^{\text{T}}.$$

(35)

The total slip rate can be expressed using the weights w^K in the form $\dot{\gamma} = \sum_K w^K \dot{\gamma}_{\text{eff}}^K$.

Assuming the standard two-parameter form (38) for crystallographic slip-systems, the hardening moduli matrix for effective slip-systems was derived by Lewandowski and Stupkiewicz [55]:

Table 1 Notation of positive slip-systems, directions and planes in 3D fcc crystals model, following [90]	$a1$	$a2$	$a3$	$b1$	$b2$	$b3$	$c1$	$c2$	$c3$	$d1$	$d2$	$d3$
	$[0\bar{1}1]$	$[10\bar{1}]$	$[\bar{1}10]$	$[011]$	$[\bar{1}0\bar{1}]$	$[1\bar{1}0]$	$[0\bar{1}1]$	$[\bar{1}0\bar{1}]$	$[110]$	$[011]$	$[10\bar{1}]$	$[\bar{1}\bar{1}0]$
			(111)			$(\bar{1}\bar{1}1)$			$(\bar{1}11)$			$(1\bar{1}1)$

Table 2 Effective in-plane slip-systems K, respective sums of α systems, directions $\mathbf{s}_{\text{eff}}^K$ and planes $\mathbf{m}_{\text{eff}}^K$ for 2D plane-strain deformation in the (1 1 0) plane

K	1	2	3	4	5	6
	$d2 + d\bar{1}$	$a\bar{3} + b3$	$c\bar{2} + c1$	$d\bar{2} + d1$	$a3 + b\bar{3}$	$c2 + c\bar{1}$
$\mathbf{s}_{\text{eff}}^K$	$[1\bar{1}\bar{2}]$	$[1\bar{1}0]$	$[\bar{1}1\bar{2}]$	$[\bar{1}12]$	$[\bar{1}10]$	$[1\bar{1}2]$
$\mathbf{m}_{\text{eff}}^K$	$(1\bar{1}1)$	(001)	$(1\bar{1}\bar{1})$	$(1\bar{1}1)$	(001)	$(1\bar{1}\bar{1})$

$$\left(h_{\text{eff}}^{KL}\right) = h \begin{pmatrix} \mathbb{Q}_{3\times3} & \mathbb{Q}_{3\times3} \\ \mathbb{Q}_{3\times3} & \mathbb{Q}_{3\times3} \end{pmatrix}, \tag{36}$$

$$\mathbb{Q}_{3\times3} = \begin{pmatrix} \frac{2}{3}(1+q) & 2q & \frac{4}{3}q \\ 2q & \frac{3}{2}(1+q) & 2q \\ \frac{4}{3}q & 2q & \frac{2}{3}(1+q) \end{pmatrix}, \tag{37}$$

where the latent-to-self hardening ratio q and the hardening modulus h are to be specified.

The effective slip-systems interaction matrix (g_{eff}^{KL}) takes the form analogous to Eq. (8), $g_{\text{eff}}^{KL} = h_{\text{eff}}^{KL} + \mathbf{p}_{\text{eff}}^K \cdot \mathbb{C}_{\text{eff}}^{\text{e}} \cdot \mathbf{p}_{\text{eff}}^L$, where the constant elastic stiffness tensor $\mathbb{C}_{\text{eff}}^{\text{e}}$ is defined in reference to the crystal orientation chosen.

6 Rate-independent versus rate-dependent results—numerical examples

6.1 Material properties

Numerical simulations have been performed for a (fcc) copper single crystal with constant elastic stiffness tensor $\mathbb{C}^{\text{e}}$ and saturation-type strain-hardening in the form (39) at room temperature.

The symmetric hardening moduli matrix $(h^{\alpha\beta})$ for slip systems has been specified in the standard two-parameter form

$$h^{\alpha\beta} = h\left(q + (1-q)\,\delta^{\alpha\beta}\right), \tag{38}$$

where q is the latent-to-self hardening ratio, usually taken from the range $1 \le q \le 1.4$ after [40], and $\delta^{\alpha\beta}$ is the Kronecker symbol. Isotropic hardening modulus h is defined by [10]

$$h = h_0 \left(1 - \frac{\tau_{\text{cr}}}{\tau_{\text{s}}}\right)^a \qquad \text{for } \tau_0 \le \tau_{\text{cr}} \le \tau_{\text{s}}, \tag{39}$$

with initial hardening parameter h_0, saturation stress τ_{s} and exponent a as constant parameters. Isotropic critical flow-stress rate is defined as $\dot{\tau}_{\text{cr}} = h\dot{\gamma}$, where $\dot{\gamma} = \sum_\alpha |\dot{\gamma}^\alpha|$ is the rate of total accumulated slip γ. The initial critical stress at $\gamma = 0$ equals $\tau_{\text{cr}} = \tau_0$. Integration over time gives (cf. [11])

$$\tau_{\text{cr}}(\gamma) = \tau_{\text{s}} - \tau_{\text{s}}\left(A + B\,\gamma\right)^{\frac{1}{1-a}} \qquad \text{for } a \ne 1, \tag{40}$$

with two constant parameters $A = \left(1 - \frac{\tau_0}{\tau_{\text{s}}}\right)^{1-a}$ and $B = \frac{(a-1)h_0}{\tau_{\text{s}}}$ and $\gamma = \int \sum_\alpha |\dot{\gamma}^\alpha|\,\mathrm{d}t$.

The values of constant elastic moduli (C_{11}, C_{12}, C_{44}) that define elastic stiffness tensor $\mathbb{C}^{\text{e}}$ for Cu of cubic symmetry, taken after [88], and the hardening parameters used in all simulations reported in this paper are listed in Table 3. In what follows, the key parameter is $q > 1$.

Additionally, in computations for the power-law rate-dependent (RD) regularization, Eq. (31), the reference slip-rate $\dot{\gamma}_0 = 10^{-3}$ 1/s was used throughout.

6.2 Results for uniform deformation

During FE calculations using adaptive time step Δt, the difference quotient of the imposed external strain increment $\Delta\bar{\varepsilon}$ to Δt has been adjusted so that the influence of the rate-sensitivity exponent, m or its inverse r in Eq. (31), be negligible for uniform deformation. This has been done as follows, separately for uniform plane-strain compression (or tension) and pure shear. In both cases, only two slip-systems γ_{eff}^1 and γ_{eff}^6 are active. (Recall that the superscripts $K = 1, \ldots, 6$ represent the labels of the effective in-plane slip-systems, not any exponent.)

In the case of uniform plane-strain compression along x_2 axis in the orientation $\omega = 0$, the total strain rate is approximately equal to the plastic strain rate and has two non-zero components, $\dot{\varepsilon}_{22} \cong -\dot{\varepsilon}_{11}$. The plastic strain rate in the compression direction is $\dot{\varepsilon}_{22}^{\text{p}} = -\frac{\sqrt{2}}{3}(\dot{\gamma}_{\text{eff}}^1 + \dot{\gamma}_{\text{eff}}^6)$, with $\dot{\gamma}_{\text{eff}}^1 = \dot{\gamma}_{\text{eff}}^6 \ge 0$ and $\tau_{\text{eff}}^1 = \tau_{\text{eff}}^6 = -\frac{\sqrt{2}}{3}\sigma_{22}$. Assuming the value of the shear rate on the active slip-systems $\dot{\gamma}_{\text{eff}}^1 = \dot{\gamma}_{\text{eff}}^6 = \dot{\gamma}_0 = 0.001$ 1/s, so that the compressive plastic strain rate is $\dot{\varepsilon}_{22}^{\text{p}} = -\frac{2\sqrt{2}}{3}\dot{\gamma}_0 \approx -0.000943$ 1/s $= \Delta\varepsilon_{22}^{\text{p}}/\Delta t$, we get $\left(|\tau_{\text{eff}}^K|/\tau_{\text{cr-eff}}^K\right)^{1/m} = 1$ for any value of exponent m.

A similar procedure applied to pure shear, but in the case of orientation $\omega = \pi/4$, leads analogously to the conclusion that $\dot{\varepsilon}_{12}^{\text{p}} = \frac{\sqrt{2}}{3}(\dot{\gamma}_{\text{eff}}^1 + \dot{\gamma}_{\text{eff}}^6) = 0.000943$ 1/s implies $\left(|\tau_{\text{eff}}^K|/\tau_{\text{cr-eff}}^K\right)^{1/m} = 1$ for any value of exponent m. The difference between these two cases, apart from the irrelevant hydrostatic stress component, lies in the different mutual orientation of the crystal and FE mesh as well as the differently imposed boundary conditions.

Effectiveness of the above procedure to set the external strain-rate $\Delta\bar{\varepsilon}/\Delta t$ has been verified numerically by com-

Table 3 Material parameters of a pure copper crystal used in the simulations

C_{11} (GPa)	C_{12} (GPa)	C_{44} (GPa)	τ_0 (MPa)	τ_s (MPa)	h_0 (MPa)	a	q
Elastic moduli			Hardening parameters				
170	124	75	1	144	250	2	1.4

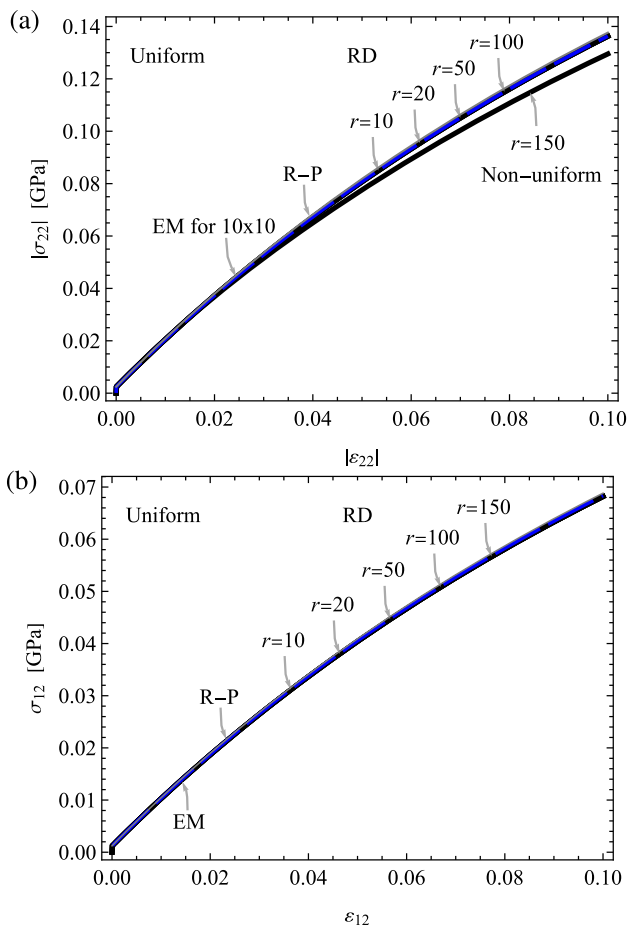**Fig. 2** Stress–strain curves in FEM simulations using the rate-dependent algorithm (RD) for selected values of exponent $r = 10, 20, 50, 100, 150$ (black curves) and using the incremental energy minimization algorithm (EM) (dashed blue curves). The uniform responses almost coincide with the upper grey curves (R-P) calculated analytically for the rigid-plastic model. (**a**) Plane-strain compression in case $\omega = 0$, for RD algorithm with 30×30 mesh and for EM algorithm with 10×10 mesh, using maximum deformation increment $|\Delta\bar{\varepsilon}_{22}|_{\max} = 10^{-4}$ and $|\Delta\bar{\varepsilon}_{22}|_{\max} = 10^{-3}$, respectively. (**b**) Pure shear in case $\omega = \pi/4$, using maximum deformation increment $2\Delta\bar{\varepsilon}_{12\,\max} = 10^{-3}$ for RD algorithm and $2\Delta\bar{\varepsilon}_{12\,\max} = 10^{-4}$ for EM algorithm, in both cases with mesh 10×10

paring the finite element results, for the rate-dependent algorithm (RD) and $r = 10, 20, 50, 100, 150$, with the rate-independent EM model. The results of RD calculations presented in Fig. 2 were performed using an automatic selection of the time step bounded from above and FE mesh density as indicated in the figure caption. The boundary conditions for plane-strain compression are described in Sect. 6.3 and

for simple shear in Sect. 6.5.1. For the coarse meshes as described in the figure caption, all the stress–strain curves in each of Fig. 2a, b merge into one curve corresponding to uniform deformation, with a notable exception in case (a) of plane-strain compression for $r = 150$, to be discussed later on.

The analytical solution for uniform deformation, assuming a rigid-plastic model, can be determined using Eqs. (38) and (40). For two equally active effective slip-systems {1, 6}, for exponent $a \neq 1$ using the formulae of 2D plane-strain model collected in Sect. 5, we obtain

$$\tau_{\text{eff}}^K(\gamma) = \tau_{\text{cr-eff}}^K(\gamma) = \tau_{0\text{-eff}}$$
$$+ \frac{\sqrt{3}\tau_s}{4}\left(A^{\frac{1}{1-a}} - (A + B\gamma)^{\frac{1}{1-a}}\right) \cdot \frac{2}{3}(1 + 3q) \quad (41)$$

for $K = 1, 6$.

Values of critical stress $\tau_{\text{cr-eff}}^K(\gamma)$ for non-active slip-systems {4, 3} (opposite to {1, 6}, cf. Fig. 1) are calculated by the same formula (41). Critical stress $\tau_{\text{cr-eff}}^K(\gamma)$ for remaining non-active slip-systems {2, 5} can be calculated by replacing the factor $\frac{2}{3}(1+3q)$ with $4q$. Total accumulated slip γ on two active slip-systems {1, 6} can be calculated using weights w^K (35) in the form $\gamma = \frac{2}{\sqrt{3}}(\gamma_{\text{eff}}^1 + \gamma_{\text{eff}}^6)$.

For plane-strain compression in x_2-direction in case $\omega = 0$, the stress $\sigma_{22}(\gamma) = -\frac{3}{\sqrt{2}}\tau_{\text{eff}}^K(\gamma)$ for $K = 1, 6$ is calculated using formula (41) with total accumulated slip $\gamma = \sqrt{6}\,|\varepsilon_{22}|$. This closed-form relationship for plane-strain compression is shown in Fig. 2a as the upper stress–strain curve (R-P). In the same way, an analogous formula $\sigma_{12}(\gamma) = \frac{3}{2\sqrt{2}}\tau_{\text{eff}}^K(\gamma)$, for $K = 1, 6$ and $\gamma = \sqrt{6}\,\varepsilon_{12}$ is obtained and illustrated in the case of pure shear in Fig. 2b.

6.3 Plane-strain compression in case $\omega = 0$

As a first example, a series of plane-strain compression simulations in the case of orientation $\omega = 0$ as shown in Fig. 1a were performed. Single crystal finite elements with slip system activity determined at the integration points using the rate-independent incremental energy minimization algorithm (EM) or the rate-dependent algorithm (RD) were applied. Regular FE meshes of various densities with square elements were used. The boundary conditions corresponding to uniform deformation were enforced by a uniform displacement on the upper edge and zero on the bottom edge in the vertical direction (x_2), leaving free deformation in the
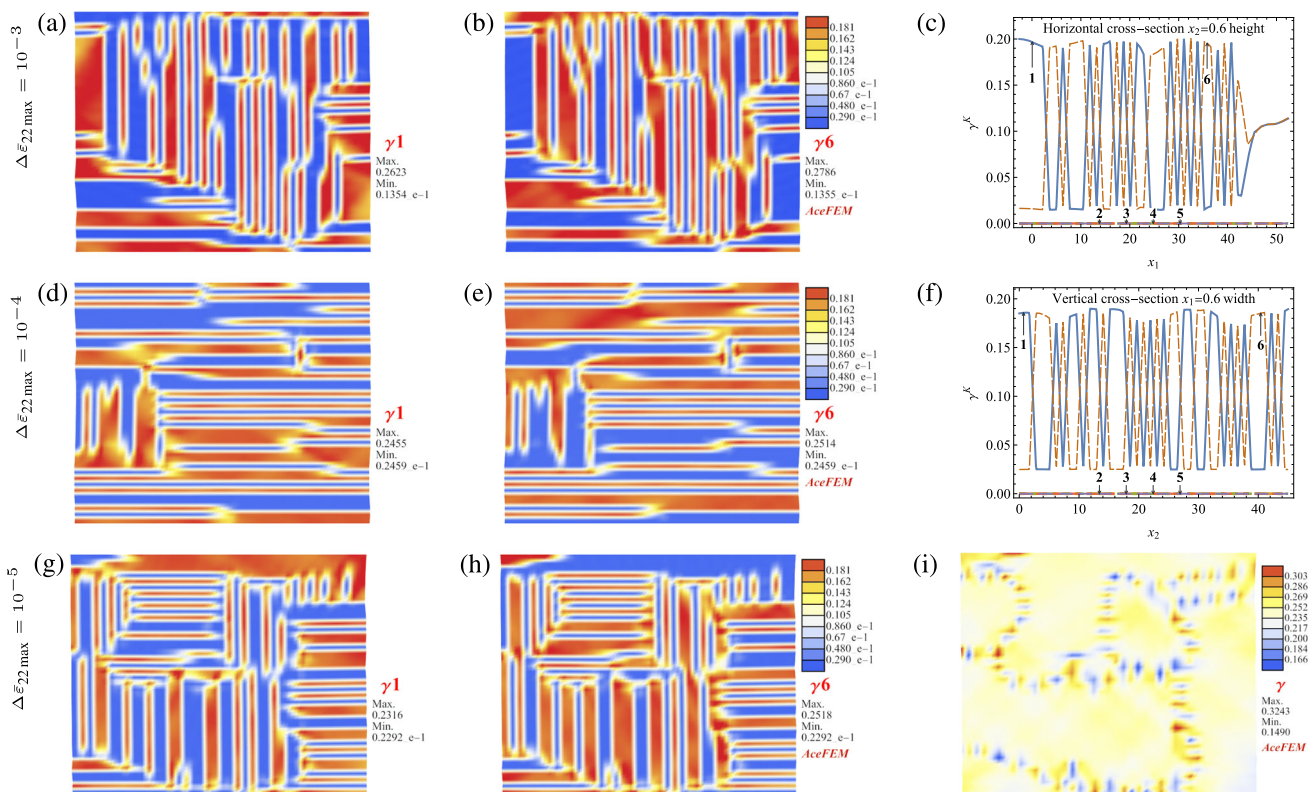
Fig. 3 Plane-strain compression in case $\omega = 0$ calculated by the incremental energy minimization algorithm (EM) for FE mesh 40×40 at final strain $\bar{\varepsilon}_{22} = 0.1$. **a**, **d**, **g** show accumulated slip γ^1, and **b**, **e**, **h** show γ^6, for maximum strain increment $\Delta\bar{\varepsilon}_{22\,\mathrm{max}} = 10^{-3}$, $\Delta\bar{\varepsilon}_{22\,\mathrm{max}} = 10^{-4}$ and $\Delta\bar{\varepsilon}_{22\,\mathrm{max}} = 10^{-5}$, respectively. **c**, **f**, **i** show activity of slip systems in horizontal cross-section, in vertical cross-section, and total accumulated slip γ, for $\Delta\bar{\varepsilon}_{22\,\mathrm{max}} = 10^{-3}$, $\Delta\bar{\varepsilon}_{22\,\mathrm{max}} = 10^{-4}$ and $\Delta\bar{\varepsilon}_{22\,\mathrm{max}} = 10^{-5}$, respectively

lateral direction (x_1). The central point of the bottom edge was clamped. A square sample was finally deformed to the *average* compressive strain $\bar{\varepsilon}_{22} = 0.1$ (for simplicity taken as positive from now on, with $\Delta\bar{\varepsilon}_{22} > 0$) varying proportionally to the control parameter. Computations have been made with adaptive step control for initial strain increment $\Delta\bar{\varepsilon}_{22} = 10^{-6}$ and minimum strain increment $\Delta\bar{\varepsilon}_{22} = 10^{-10}$. The results below are shown for 2D effective quantities but for brevity the subscript $_{\mathrm{eff}}$ has been omitted.

6.3.1 Results for rate-independent algorithm (EM)

The effect of the maximum increment in compressive strain in the range $\Delta\bar{\varepsilon}_{22\,\mathrm{max}} = 10^{-2} \div 10^{-5}$ is shown in Fig. 3 obtained for the FE mesh 40×40 using the incremental energy minimization algorithm (EM). The picture for maximum strain increment $\Delta\bar{\varepsilon}_{22\,\mathrm{max}} = 10^{-2}$ is omitted as it gives uniform deformation such that both slip-systems γ^1 and γ^6 are active in the entire sample. For the maximum strain increment in the range $\Delta\bar{\varepsilon}_{22\,\mathrm{max}} = 10^{-3} \div 10^{-5}$, the slip system activity becomes non-uniform with clearly visible horizontal and vertical bands with only one slip-system active, either

γ^1 or γ^6, separated by thin transition zones influenced by interpolation built into the system, as discussed below. The resulting pattern and the number and width of the bands are to some extent random and can even become different in subsequent computations under the same conditions, but retain their overall character. The character of already formed bands is slightly dependent on the step length (for a given FE mesh density). Changes in slip-systems shear values γ^α are shown in Fig. 3c, f in selected horizontal and vertical cross-sections using the FE shape functions. The lower bound of the accumulated slip-systems shear values is not zero due to an initial period of double slip when deformation bands have not yet been formed. Figure 3i shows that the field of total accumulated slip $\gamma = \int \dot{\gamma}\, \mathrm{d}t$ is almost uniform despite strong spatial variations in activity of individual slip systems.

The apparent gradient in Fig. 3 and others is due to the interpolation built into the AceFEM system used. To further investigate how the system automatically generates the γ^K fields, a cross-section through the integration points and for a coarser FE mesh 20×20 is shown in Fig. 4. Each dot in Fig. 4c represents a value of the incremental slip $\Delta\gamma^1$ or $\Delta\gamma^6$ calculated by EM algorithm for a single integration point, and
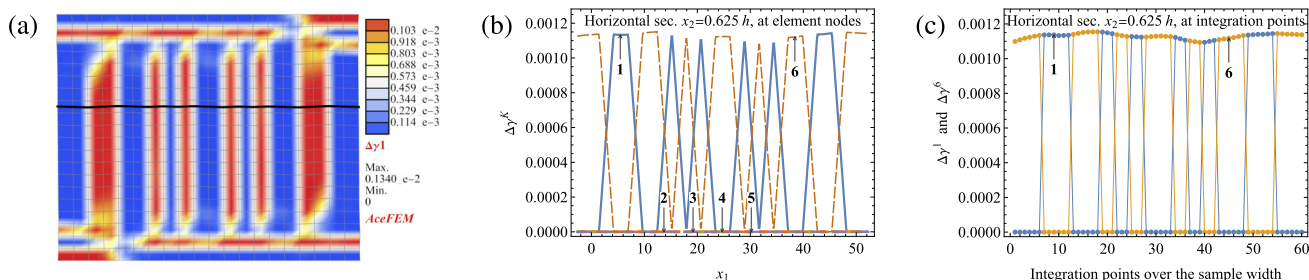
Fig. 4 Plane-strain compression in case $\omega = 0$ calculated by the incremental energy minimization algorithm (EM) for FE mesh 20×20 and maximum average strain increment $\Delta\bar{\varepsilon}_{22\,\mathrm{max}} = 10^{-3}$ at final strain $\bar{\varepsilon}_{22} = 0.1$. **a** Field of incremental slip $\Delta\gamma^1$ with marked deformed mesh and horizontal cross-section line at $x_2 = 0.625\,h$ of sample height. **b** Incremental slips $\Delta\gamma^K$ in the horizontal cross-section interpolated by AceFEM at element nodes. **c** Values of non-zero incremental slips $\Delta\gamma^1$ and $\Delta\gamma^6$ calculated at integration points in the same cross-section

three consecutive integration points belong to a single finite element. The plot of slip increments $\Delta\gamma^K$ per integration point in Fig. 4c shows a negligible gradient through a single element and a jump across the element boundary. Hence, the gradient visible in Fig. 4b is only apparent.

The influence of FE mesh density on the formation of bands and CPU time is presented in Table 4. The results are for two values of maximum strain increment in the compression direction, $\Delta\bar{\varepsilon}_{22\,\mathrm{max}} = 10^{-4}$ and $\Delta\bar{\varepsilon}_{22\,\mathrm{max}} = 10^{-3}$. The computation CPU time depends on the number of bands formed, which can be observed for rate-independent EM algorithm in Table 4 as well as in other simulations. In the particular case of uniform deformation the computations are very fast, but if many vertical and horizontal bands are created then the calculations take much longer time. However, at a certain point in the calculations, when the pattern of slip bands distribution is clear, i.e. the whole body is divided into subregions in which only a single slip is active, the computations are fast and are performed with a fairy large global Newton step.

In the case of smaller strain increment $\Delta\bar{\varepsilon}_{22\,\mathrm{max}} = 10^{-4}$, the deformation character for different FE mesh densities does not change significantly, and patterns of horizontal and vertical bands emerge for all examined FE meshes. For the larger strain increment $\Delta\bar{\varepsilon}_{22\,\mathrm{max}} = 10^{-3}$, the deformation character depends on mesh density, starting from uniform deformation for coarse mesh 10×10. For meshes 20×20 and 30×30, only horizontal bands appear or dominate, and both horizontal and vertical bands appear for mesh 40×40. For the finer meshes 80×80 and 160×160, the deformation character is similar for both maximum strain increments $\Delta\bar{\varepsilon}_{22\,\mathrm{max}} = 10^{-4}$ and $\Delta\bar{\varepsilon}_{22\,\mathrm{max}} = 10^{-3}$. As the FE mesh becomes finer, the number of bands increases and the bands become narrower as shown in Fig. 5, which is the expected effect of the lack of an internal length scale in the material model used here. For the coarser meshes up to 30×30 mesh, the character of deformation bands depends more on the deformation step length. For the finer meshes, starting

from 40×40, the character of deformation bands did not change significantly and the patterns with both vertical and horizontal bands formed for different strain increments. In contrast to the deformation bands visible on the slip distribution images, the total accumulated slip for different mesh densities and deformation step lengths is quite homogeneous and of a similar nature, as shown in Figs. 3i and 5b, d.

6.3.2 Results for rate-dependent algorithm (RD)

Guided by the above results for rate-independent (EM) modelling, computations using rate-dependent algorithm (RD) have been performed for selected values of exponent $r = 20, 50, 100, 120, 150$ and maximum strain increment $\Delta\bar{\varepsilon}_{22\,\mathrm{max}} = 10^{-4}$, Fig. 6a–d. Based on the analysis in Sect. 6.2, the external compression rate $\dot{\bar{\varepsilon}}_{22} = 0.000943$ 1/s was applied in order to reduce the influence of exponent r. The most essential conclusion is that for the parameter values up to approximately $r = 100$ the bands are not observed. They form in the case of approximately $r = 120$, and for $r = 150$ they are clearly observed and become a permanent element of the solution, as in the case of the results for the incremental energy minimization algorithm (EM), Fig. 6e–h. In the analysed examples of plane-strain compression calculated by the rate-independent algorithm (EM), only for the larger maximum strain increment $\Delta\bar{\varepsilon}_{22\,\mathrm{max}} = 10^{-2}$ deformation bands are not observed, Fig. 6e, but for the remaining step sizes the bands of a similar character appeared.

The computation CPU time and the deformation character for different FE mesh density (from 10×10 to 160×160), exponents $r = 20, 50, 100, 150$ and maximal deformation steps $\Delta\bar{\varepsilon}_{22\,\mathrm{max}} = 10^{-4}$ and 10^{-3} are summarized in Table 5. For the exponent values up to approximately $r = 100$ the bands are not observed independently of the FE mesh density and of the length of maximal strain increment. Deformation bands appear for computations with the exponent $r = 150$ (bands are also observed for $r = 100$ but for finer meshes and a larger strain increment) but their character may be different

Table 4 Summary of CPU time and deformation character for computations using the incremental energy minimization algorithm (EM) for two values of maximum strain increment $\Delta\bar{\varepsilon}_{22\,\mathrm{max}} = 10^{-4}$ and $\Delta\bar{\varepsilon}_{22\,\mathrm{max}} = 10^{-3}$

FE mesh	CPU time for $\Delta\bar{\varepsilon}_{22\,\mathrm{max}} = 10^{-4}$	Deformation character	CPU time for $\Delta\bar{\varepsilon}_{22\,\mathrm{max}} = 10^{-3}$	Deformation character
10 × 10	1 m 25 s	Horizontal or vertical bands	7 s	Uniform deformation
20 × 20	2 m 36 s	Horizontal and vertical bands	1 m 19 s	Horizontal bands
30 × 30	4 m 5 s	Horizontal and vertical bands	2 m 34 s	Horizontal bands
40 × 40	7 m 48 s	Horizontal and vertical bands	7 m 36 s	Horizontal and vertical bands
80 × 80	48 m 1 s	Horizontal and vertical bands	36 m 36 s	Horizontal and vertical bands
160 × 160	2 h 34 m 24 s	Horizontal and vertical bands	3 h 32 m 29 s	Horizontal and vertical bands

The effect of FE mesh density and maximum strain increment on the formation of deformation bands in plane-strain compression in case $\omega = 0$

and depends largely on the FE mesh density and the step length. CPU time for the exponent $r = 150$, where bands has been formed, can be compared with CPU time for the rate-independent algorithm EM given in Table 4. It can be seen that for coarse FE meshes up to 40×40 the CPU time of RD and EM computations is comparable, or RD takes slightly less time, but for finer FE meshes 80×80 and 160×160 the EM computations are faster than RD.

Computations for various maximum strain increments $\Delta\bar{\varepsilon}_{22\,\mathrm{max}} = 10^{-2} \div 10^{-5}$ have been performed in order to investigate the effect of this parameters on the formation of deformation bands using the RD algorithm, Fig. 7. The simulations were performed for FE mesh 40×40 and with exponent $r = 150$. The results of simulations for a step length of $\Delta\bar{\varepsilon}_{22\,\mathrm{max}} = 10^{-2}$ do not show clear deformation bands and are not included here. Simulations for step length $\Delta\bar{\varepsilon}_{22\,\mathrm{max}} = 10^{-3}$ show the formation of vertical bands, of a different nature than in the (EM) case, cf. Fig. 3, where both vertical and horizontal bands occurred and were much more dense. Distribution of slip-system shear $|\gamma^3|$ for the RD algorithm, shown in Fig. 7b, e, h, can be compared with shear γ^6 for the rate-independent ED algorithm, cf. Figure 3b, e, h. Computations for shorter step lengths $\Delta\bar{\varepsilon}_{22\,\mathrm{max}} = 10^{-4}$ and 10^{-5} consistently form vertical deformation bands, with the width of the bands comparable to the size of the FE elements. The fields of total accumulated slip γ for analysed step lengths are quite uniform despite visible non-uniform character of deformation bands, Fig. 7c, f, i.

Computations were also repeated for more dense meshes 80×80 and 160×160, using exponent $r = 150$ and step size $\Delta\bar{\varepsilon}_{22\,\mathrm{max}} = 10^{-4}$. The bands with alternate activity of different slip systems are formed, similarly to Fig. 7d, e and are therefore not shown here. In comparison to the previous results in Fig. 7f, the total accumulated slip γ is more uniform. Both meshes produce vertical bands which become finer with the increasing FE mesh density. As expected, rate sensitivity does not provide regularization in this respect. However, as shown in the next section, the 'macroscopic' response is almost insensitive to the mesh density if the bands have appeared.

6.3.3 Deformation band formation: Discussion

The emergence of bands with alternating activity of different slip systems is obviously related to different deformations in the bands, as illustrated in Fig. 8.

Two basic observations result from the simulations performed:

(i) Under conditions that could result in perfectly uniform strain, a deformation band pattern spontaneously emerges in the case $q > 1$ if the numerical factors discussed below allow it.
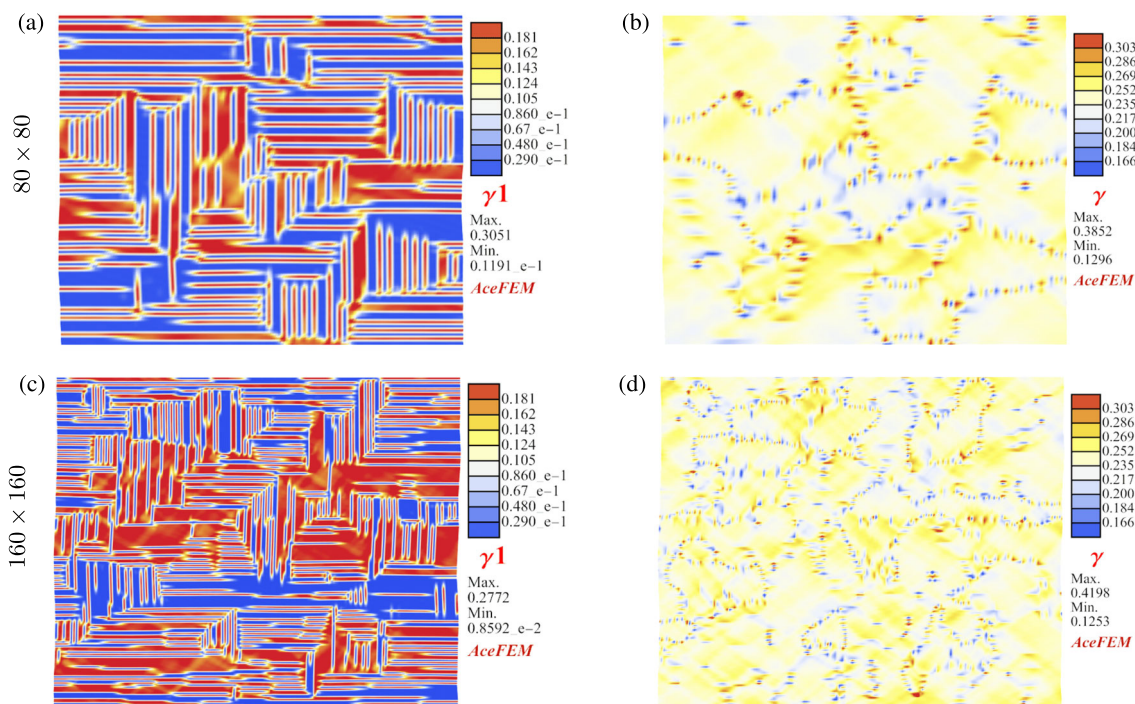
Fig. 5 Plane-strain compression in case $\omega = 0$ calculated by the incremental energy minimization algorithm (EM) for maximum strain increment $\Delta\bar{\varepsilon}_{22\,\mathrm{max}} = 10^{-3}$ and FE mesh **a, b** 80×80 and **c, d** 160×160. **a, c** Accumulated slip γ^1 and **b, c** total accumulated slip γ for final strain $\bar{\varepsilon}_{22} = 0.1$
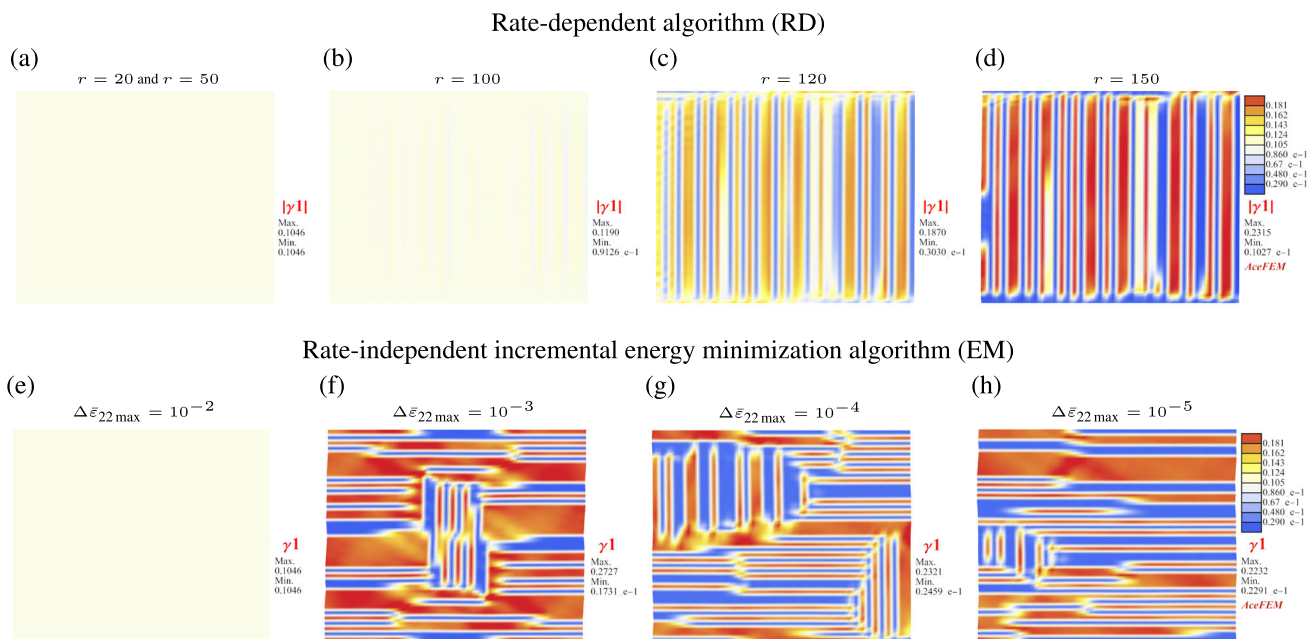
Fig. 6 **a–d** Slip-system shear $|\gamma^1|$ calculated for plane-strain compression in case $\omega = 0$ at final strain $\bar{\varepsilon}_{22} = 0.1$ using the rate-dependent algorithm (RD) for selected values of exponent $r = 20, 50, 100, 120, 150$ and maximum strain increment $\Delta\bar{\varepsilon}_{22\,\mathrm{max}} = 10^{-4}$. **e–h** For comparison, slip-system shear γ^1 calculated by the rate-independent algorithm (EM) for selected values of increment $\Delta\bar{\varepsilon}_{22\,\mathrm{max}} = 10^{-2} - 10^{-5}$. The simulations have been performed for FE mesh density 40×40

Table 5 Summary of CPU time and deformation character for computations using the rate-dependent algorithm (RD)

FE mesh	$\Delta\bar{\varepsilon}_{22\,max}$	Exponent r	CPU time	Deformation character
10×10	10^{-4}	20	1 m 23 s	Uniform deformation
40×40			3 m 51 s	
80×80			11 m 43 s	
160×160			48 m 31 s	
10×10	10^{-3}	20	8 s	Uniform deformation
40×40			24 s	
80×80			1 m 16 s	
160×160			5 m 11 s	
10×10	10^{-4}	50	1 m 21 s	Uniform deformation
40×40			3 m 42 s	
80×80			12 m 17 s	
160×160			48 m 52 s	
10×10	10^{-3}	50	8 s	Uniform deformation
40×40			24 s	
80×80			1 m 23 s	
160×160			6 m 15 s	
10×10	10^{-4}	100	1 m 14 s	Uniform deformation
40×40			3 m 35 s	
80×80			16 m 55 s	
160×160			3 h 6 m 49 s	
10×10	10^{-3}	100	9 s	Uniform deformation
40×40			1 m 13 s	
80×80			29 m 33 s	Vertical bands
160×160			5 h 31 m 24 s	Vertical bands
10×10	10^{-4}	150	1 m 27 s	Horizontal bands
40×40			7 m 7 s	Vertical bands
80×80			48 m 28 s	Vertical bands
160×160			8 h 39 m 44 s	Vertical bands
10×10	10^{-3}	150	14 s	Horizontal bands
40×40			2 m 33 s	Horizontal and vertical bands
80×80			1 h 0 m 53 s	Horizontal and vertical bands
160×160			6 h 26 m 26 s	Horizontal and vertical bands

The effect of FE mesh density, strain-rate sensitivity and maximum strain increment on the formation of deformation bands in plane-strain compression in case $\omega = 0$ at final strain $\bar{\varepsilon}_{22} = 0.1$

(ii) In the case of plane-strain compression, which could lead to the uniform activity of two effective slip systems {1, 6}, the deformation domain is covered by two families of vertical or horizontal bands, with one slip system predominant in one family of bands and the other slip system predominant in another family of bands.

Observation (i) can be explained by referring to the so-called yield-vertex effect. Consider a cross-section of the current yield surface $f^K = 0$ in stress space in vicinity of the corner formed by the two segments corresponding to the currently equally active two slip systems, say for $K = 1, 6$. In accordance with a general analysis of uniqueness [73], fulfillment of the condition $\det(h_{\text{eff}}^{KL}) < 0$, which reduces here to $q > 1$ for $h > 0$, implies that a further increment in compressive stress, $\Delta\sigma_{22}$, can be associated with the incremental activity of both slip systems or only one slip system. In the latter case, if the self-hardening of one active slip system is less than latent hardening of the other slip system due to $q > 1$, the other slip system undergoes unloading and becomes inactive. If this is associated with a local change in the direction of strain increment which can be kinematically compatible with neighbouring elements in the discretization scheme used, then it can lead to non-uniform deformation.

The explanation for observation (ii) is related to the question of whether such a local change in the direction of strain increment mentioned above can be accommodated by the surrounding material elements during FE computations. In the plane strain problem under consideration, this can be done in
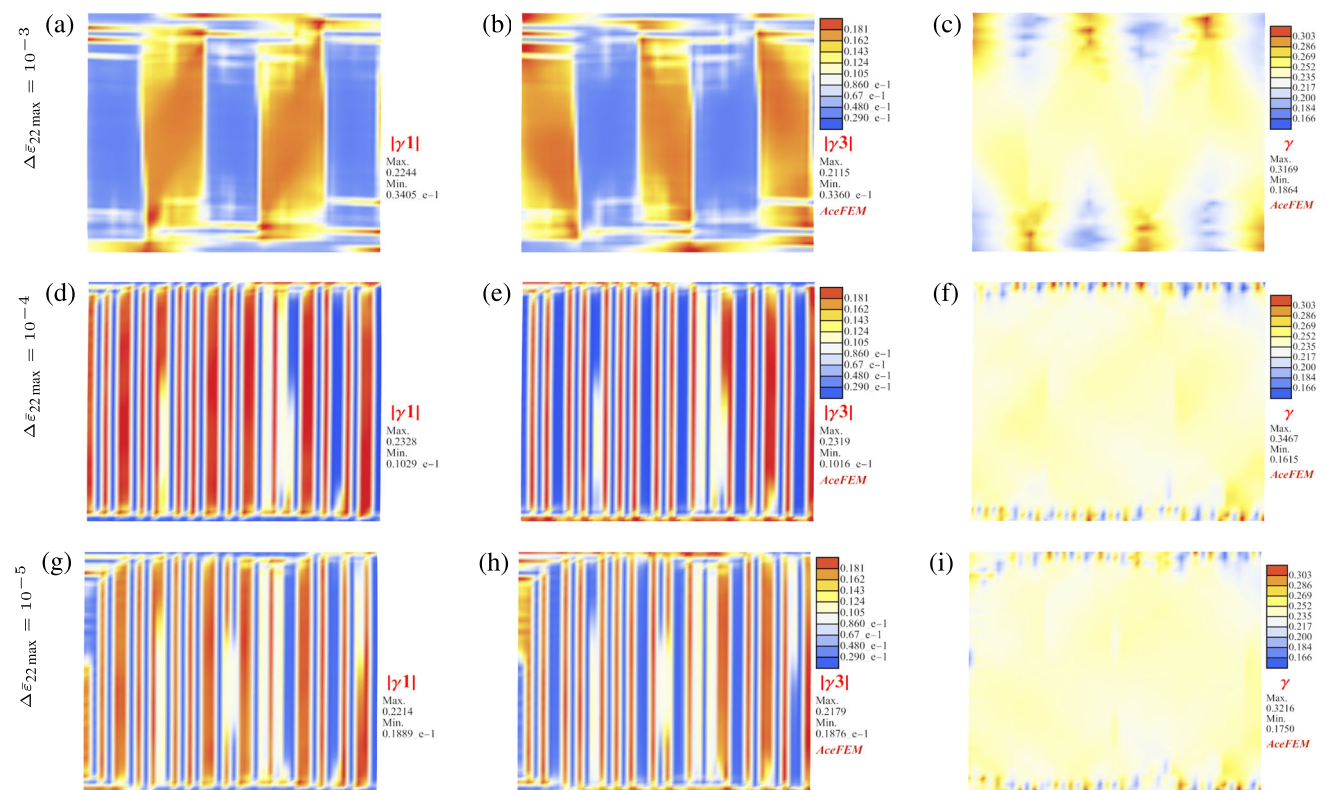
Fig. 7 Results for plane-strain compression in case $\omega = 0$ calculated by the rate-dependent algorithm (RD) with exponent $r = 150$ at final strain $\bar{\varepsilon}_{22} = 0.1$ for FE mesh 40×40. **a, d, g** Slip-system shear $|\gamma^1|$, **b, e, h** $|\gamma^3|$, and (c, f, i) total accumulated slip γ for maximum strain increment (**a–c**) $\Delta\bar{\varepsilon}_{22\,\mathrm{max}} = 10^{-3}$, (**d–f**) $\Delta\bar{\varepsilon}_{22\,\mathrm{max}} = 10^{-4}$ and (**g–i**) $\Delta\bar{\varepsilon}_{22\,\mathrm{max}} = 10^{-5}$, respectively

two ways: (a) for vertical bands and (b) for horizontal bands, which follows from the requirement of equal longitudinal strain of the band interface from both sides. Due to the symmetries involved, it is clear, even without calculation, that both kinematic and statical consistency is preserved in each case (a) or (b), thus completing the explanation of (i) above. In the small strain formalism used, the horizontal and vertical orientations are equivalent because the total stress itself is not present in the incremental formulation of the banding problem.

Based on the FE calculations performed, several factors that determine whether bands form or not can be specified as follows.

The basic factor, as explained above, is the latent-to-self hardening ratio $q > 1$; in simulations with $q < 1$, no deformation bands were observed in the FE simulations carried out.

Another factor is the orientation of the crystallographic lattice with respect to the applied loading scheme, because at least two slip systems need to be activated simultaneously for the yield-vertex effect to occur, cf. the explanation to (i).

If these two conditions are satisfied then the spontaneous formation of band microstructure can be triggered by numer-

ical inaccuracies that are inevitable during calculations. It is emphasized that the computational model used in this work does not have an implemented laminate at the local level of an integration point or any built-in artificial imperfections.

As the essential specific outcome of the FE calculations performed using the rate-dependent algorithm (RD), a threshold value of the rate sensitivity exponent m has been identified as $r = 1/m = 100 \div 150$. At values of r below this range (higher rate-sensitivity), no bands were observed. Together with the other factors discussed above, this may help to understand why deformation banding is not a common feature in field simulations of the rate-dependent deformation of metal single crystals reported so far in the literature.

The next factor is the type of the FE mesh used in the simulations, here with a square element shape and biquadratic shape functions with (3×3) Gauss quadrature points. It is difficult to clearly determine the FE mesh density needed for the band formation. The influence of the deformation step length was also observed. However, since adaptive time step control was used in FE calculations, the deformation step lengths given here refer to their maximum allowable values. In the case of simulations performed for a larger strain step $\Delta\bar{\varepsilon}_{22\,\mathrm{max}} = 10^{-2}$, bands were not created. Bands
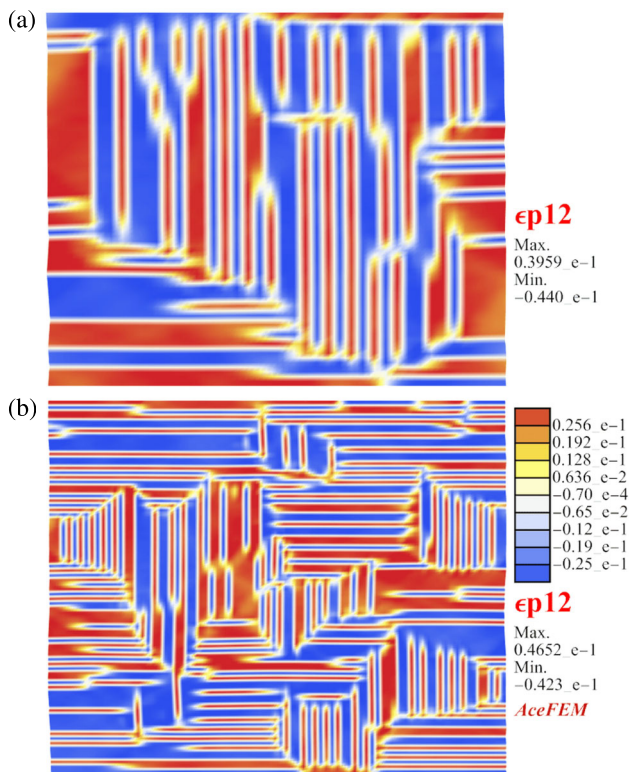
(a)

(b)

Fig. 8 Plane-strain compression in case $\omega = 0$ calculated by the rate-independent (EM) algorithm for maximum strain increment $\Delta\bar{\varepsilon}_{22\,max} = 10^{-3}$ and final strain $\bar{\varepsilon}_{22} = 0.1$. Fields of plastic strain ε_{12}^{p} for FE mesh **a** 40×40 (results from Fig. 3a–c) and **b** 80×80 (results from Fig. 5a, b)

Fig. 9 The average stress versus average strain curve in plane-strain compression in case $\omega = 0$ is insensitive to the mesh density among the selected FE mesh densities: $20^2, 40^2, 80^2, 160^2$. The stress–strain curves were calculated by **a** the rate-independent incremental energy minimization algorithm (EM) and by **b** the rate-dependent algorithm (RD) with exponent $r = 150$, both using maximum deformation increment $\Delta\bar{\varepsilon}_{22\,max} = 10^{-4}$. The additionally inserted fields of the slip-system shear γ^1 correspond to the outermost meshes, 20^2 and 160^2, for final strain $\bar{\varepsilon}_{22} = 0.1$

were formed for step length $\Delta\bar{\varepsilon}_{22\,max} = 10^{-3}$ or smaller. In the analyzed examples, the final compressive strain does not exceed 0.1.

If the conditions characterized above for formation of deformation bands are satisfied, then the width of individual bands is strongly correlated with the mesh density in the FE simulations. This has been expected because the material model used has no internal length scale. However, an important general observation is the following:

(iii) The overall response of the crystal, represented by the average stress versus average strain curve, is insensitive to the mesh density.

This is visualized in Fig. 9, where the macroscopic stress–strain curves have been calculated and compared for selected FE mesh densities: $20^2, 40^2, 80^2, 160^2$, for the rate-independent incremental energy minimization algorithm (EM) in Fig. 9a and the rate-dependent algorithm (RD) with exponent $r = 150$ in Fig. 9b. The curves for different mesh densities are almost identical, even in case of the EM algorithm, although for meshes 20^2 and 160^2 the resulting microstructures are significantly different. For both algorithms it can be concluded that the macroscopic stress–strain curve for the plane strain compression is practically
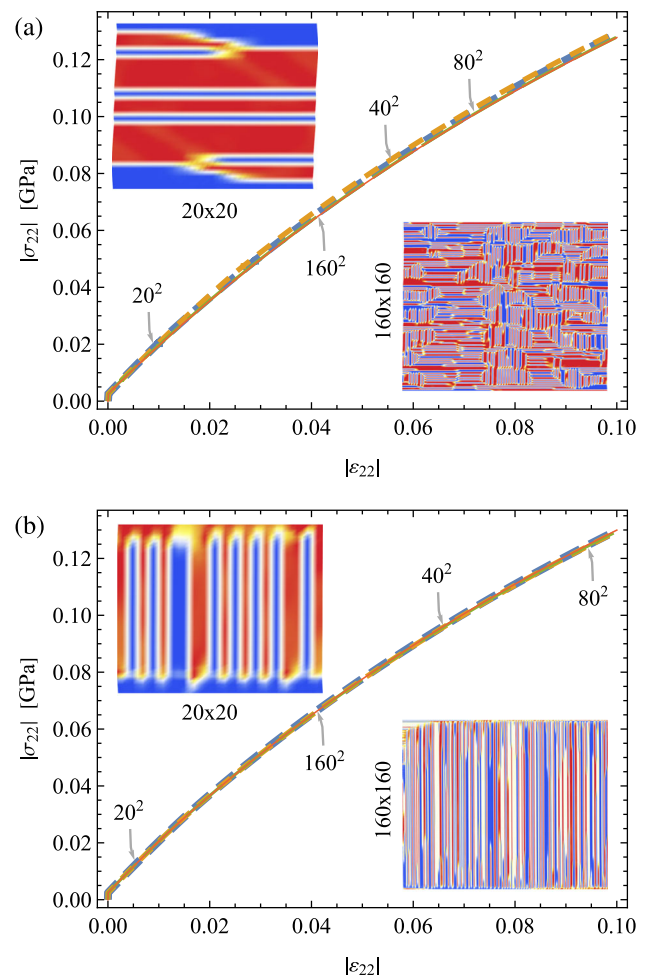
independent of the mesh density provided the conditions for the band formation have been satisfied. As it can be seen by comparison with Fig. 2a, the macroscopic curve in the case of deformation banding lies lower than that for uniform strain, independently of the mesh density. The reason for this is clear: splitting the double slip into single-slip domains reduces the overall hardening because the self-hardening of one slip system is less than the simultaneous cross-hardening of both slip systems in the case $q > 1$.

To verify band patterning conditions under circumstances not limited to the macroscopically uniform plane strain compression with FE mesh aligned bands, additional 2D examples are examined in the following sections.
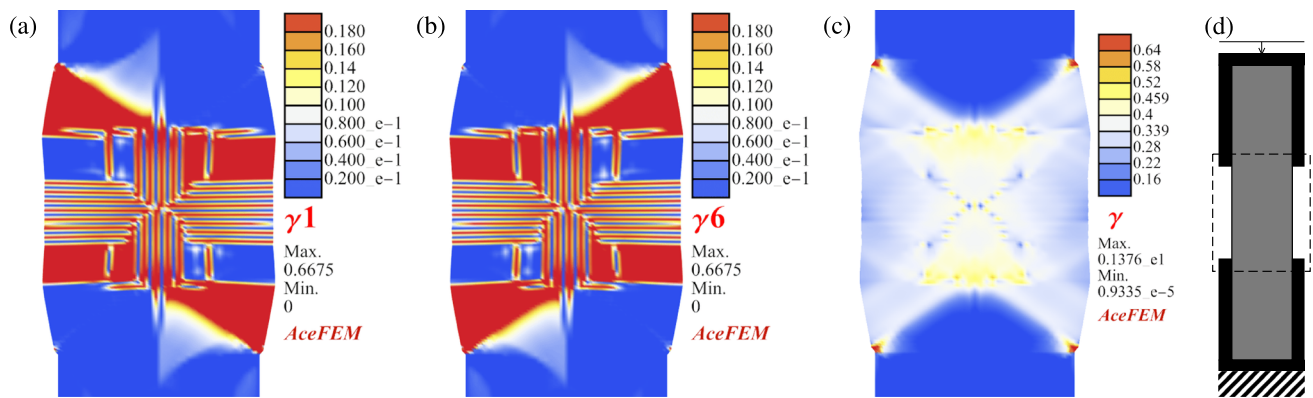
Fig. 10 Plane-strain compression of the sample clamped in rigid grips in case $\omega = 0$ calculated by incremental energy minimization algorithm (EM) for maximum average strain increment $\Delta\bar{\varepsilon}_{22\,\mathrm{max}} = 10^{-3}$ and FE mesh 40×200. Distribution of slip-system shear **a** γ^1, **b** γ^6, and **c** total accumulated slip γ. **d** Scheme of the compressed sample clamped in grips with the area shown in the adjacent figures marked by a dashed rectangle

6.4 Plane-strain compression of the sample clamped in rigid grips in case $\omega = 0$

Plane-strain compression in the vertical direction (x_2) is simulated in case of orientation $\omega = 0$. In contrast to the example from Sect. 6.3, the sample with a height-to-width ratio of 5 is now clamped in rigid grips as illustrated in Fig. 10d. The upper and lower grips have a height equal to one third of the total height of the sample. In the calculations, the upper grip is vertically lowered while the lower grip remains fixed. The final average vertical strain $\bar{\varepsilon}_{22} = 4\%$ is achieved by deformation with the maximum deformation step $\Delta\bar{\varepsilon}_{22\,\mathrm{max}} = 10^{-3}$. Square elements and regular FE meshes of various density were used, but the graphs are shown for 40×200 mesh as an illustrative result. Due to the rigid grips, the deformation is concentrated in the central part of the sample and therefore only the central part, amounting to 0.4 of the total height, is shown in Figs. 10 and 11.

Computations were performed using the incremental energy minimization algorithm (EM), Fig. 10; and the rate-dependent algorithm (RD) with exponent $r = 150$ and the average compression rate $\dot{\bar{\varepsilon}}_{22} = 0.000945 \, 1/\mathrm{s}$ of the section between the grips, Fig. 11.

The differences in the results of the EM and RD algorithms are more visible in this example. First of all, the number of bands and their width are different, the EM algorithm reveals many more of them and they are narrower than the bands generated by the RD algorithm. Additionally, the EM algorithm gives also horizontal bands, while in the case of RD they are not clearly visible, although not excluded for finer FE meshes. This latter observation is consistent with the results from the previous Sect. 6.3, where vertical bands also dominated for plane-strain compression for the RD algorithm.

The computation CPU time and the deformation character for both algorithms and various FE mesh density are summarized in Table 6.

6.5 Examples for the lattice orientation $\omega = \pi/4$

In this section, results of three types of simple shear computations are reported, all in the case of orientation $\omega = \pi/4$ shown in Fig. 1b, which can lead to shearing on two slip-systems $\{1, 6\}$ as in Sect. 6.3. However, due to different mutual orientation of the crystal and the FE mesh and the differently imposed boundary conditions, the deformation banding pattern is different. Computations reported here have been performed for the maximum increment of imposed average simple shear $\bar{\gamma}_{12} = 2\bar{\varepsilon}_{12}$ equal to $\Delta\bar{\gamma}_{12\,\mathrm{max}} = 10^{-3}$.

Simulations of simple shear $\bar{\gamma}_{12}$ for orientation $\omega = 0$ are not illustrated because they did not contain visible deformation bands, regardless of the algorithm or the FE mesh density used.

6.5.1 Macroscopically uniform simple shear, $\omega = \pi/4$

The term macroscopically uniform in the title of this Section refers only to the boundary conditions and not to the resultant deformation character with or without bands. A uniform character of deformation discussed in Sect. 6.2 has been obtained using boundary conditions specified in this Section but for a more coarse FE mesh.

Macroscopic simple shear is imposed by moving the top edge in the horizontal direction (x_1) while the bottom edge is clamped. In addition, both lateral vertical edges are assumed here to remain rectilinear while changing slope. The square sample is deformed up to the ratio of top edge displacement to sample height equal to 0.1.
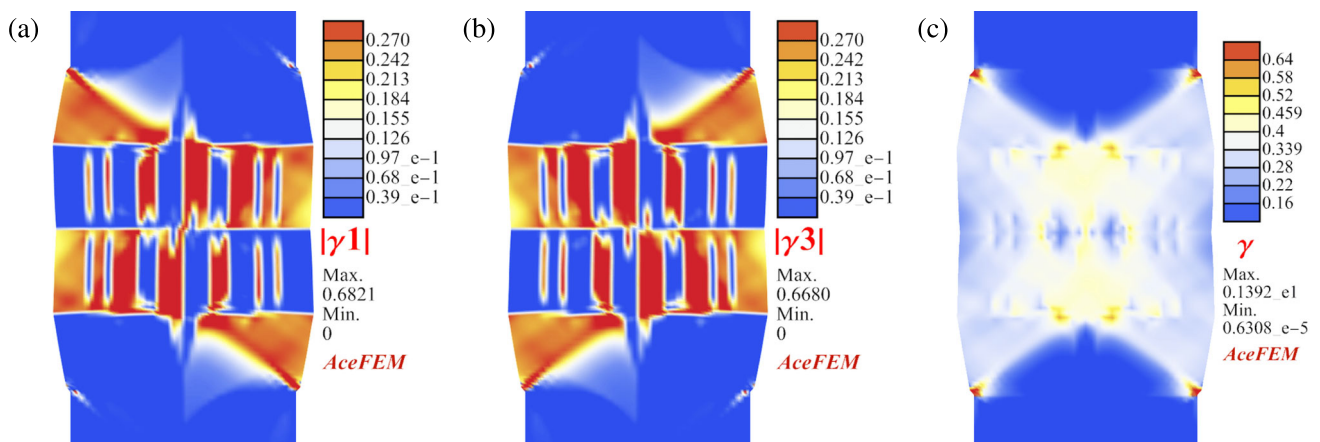
Fig. 11 Plane-strain compression of the sample clamped in rigid grips in case $\omega = 0$ calculated by rate-dependent algorithm (RD) with exponent $r = 150$ for maximum average strain increment $\Delta \bar{\varepsilon}_{22\,max} = 10^{-3}$ and FE mesh 40×200. Distribution of slip-system shear **a** $|\gamma^1|$, **b** $|\gamma^3|$, and **c** total accumulated slip γ

Table 6 Summary of the CPU time and deformation character for plane-strain compression of the sample clamped in rigid grips in case $\omega = 0$

FE mesh	CPU time for $\Delta \bar{\varepsilon}_{22\,max} = 10^{-3}$	Deformation character
Incremental energy minimization algorithm (EM)		
20×100	8 m 48 s	vertical bands
30×150	19 m 55 s	vertical and horizontal bands
40×200	39 m 28 s	vertical and horizontal bands
50×250	1 h 5 m 25 s	horizontal bands
Rate-dependent algorithm (RD)		
20×100	7 m 15 s	vertical bands
30×150	26 m 16 s	vertical bands
40×200	1 h 15 m 23 s	vertical bands
50×250	2 h 55 m 6 s	vertical bands

Computations have been performed using the incremental energy minimization algorithm (EM) and the rate-dependent algorithm (RD) with exponent $r = 150$. Calculations with maximum strain increment $\Delta \bar{\varepsilon}_{22\,max} = 10^{-3}$ up to final average strain $\bar{\varepsilon}_{22} = 0.04$, for both algorithms. The effect of FE mesh density on the formation of deformation bands is shown

Computations were performed by the incremental energy minimization algorithm (EM), illustrated in Fig. 12, and by the rate-dependent algorithm (RD) with the exponent $r = 150$ and macroscopic shear rate $\dot{\bar{\varepsilon}}_{12} = 0.000943\ 1/s$, shown in Fig. 13. The differences in results are better visible for a finer FE mesh. The RD algorithm gives a more regular character of deformation bands in contrast to disordered appearance of bands for EM algorithm.

Resulting deformation character and CPU time for various FE meshes, additionally including 160×160 mesh, summarized in Table 7, are similar for both algorithms, although the RD algorithm gives a more regular bands in contrast to disordered bands for EM algorithm. In this example, CPU time is even shorter for the RD algorithm compared to the EM algorithm.

Similar results of both algorithms have been obtained for a smaller step of simple shear $\Delta \bar{\gamma}_{12\,max} = 10^{-4}$. The results are not included in this paper.

It can be expected that the shape of mesh elements can influence the character of the bands. This can be observed by comparing the plane-strain compression results, where the bands are parallel to the grid lines, with the shear tests results above, where the bands are not aligned with the grid lines and their width is not equal to the size of the element. The computations repeated for the same data as in Fig. 12a, b but for the unstructured triangular mesh (not shown), are very similar to Fig. 12a, b, but this may not be the case in general. The issue of the influence of the mesh type on the formation of deformation bands requires a separate investigation.

6.5.2 Non-uniform simple shear, $\omega = \pi/4$

As above, the top edge is moved in the horizontal direction (x_1) and the bottom edge is clamped, but the lateral edges are now free. As in the previous Section, the final ratio of top edge displacement to sample height is equal to 0.1.
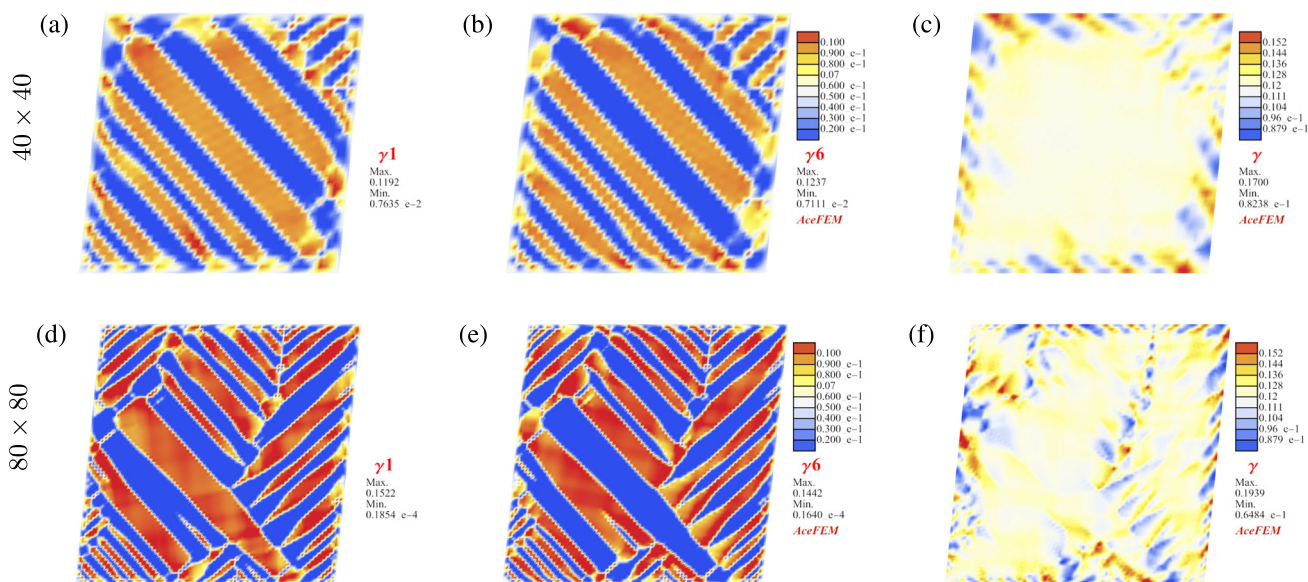
Fig. 12 Macroscopically uniform simple shear in case $\omega = \pi/4$ calculated by incremental energy minimization algorithm (EM) for the maximum increment of average simple shear $\Delta\bar{\gamma}_{12\,\mathrm{max}} = 10^{-3}$ and final macroscopic strain $\bar{\varepsilon}_{12} = 0.05$. Slip-system shear **a, d** γ^1, **b, e** γ^6 and (c, f) total accumulated slip γ for FE mesh **a–c** 40×40 and **d–f** 80×80
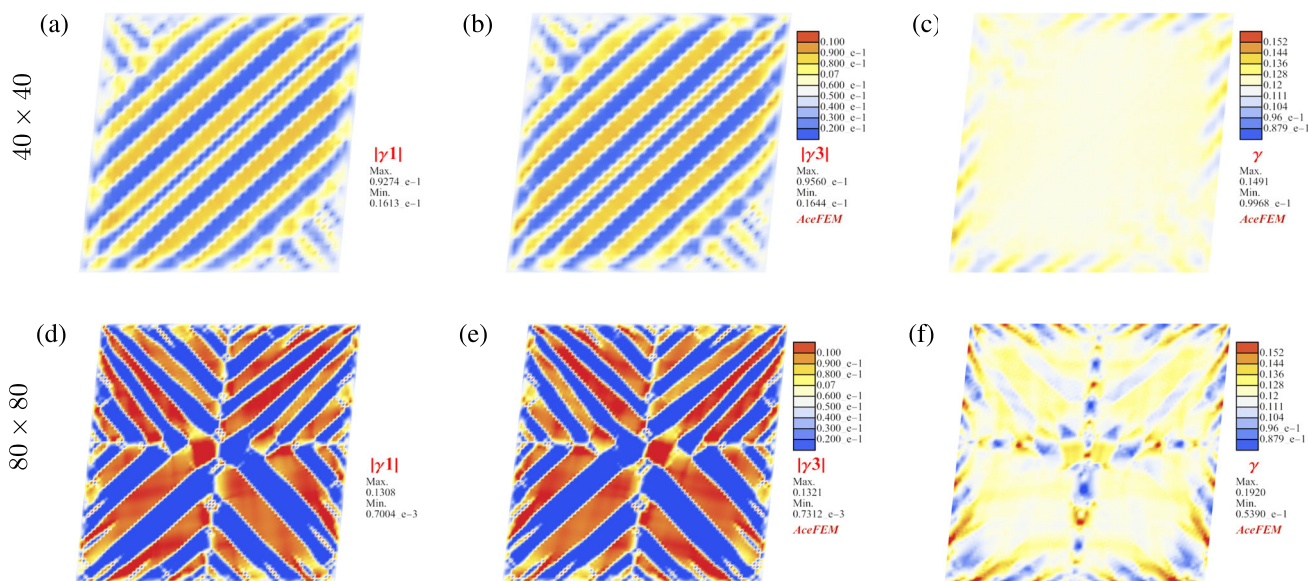
Fig. 13 Macroscopically uniform simple shear in case $\omega = \pi/4$ calculated by rate-dependent algorithm (RD) with exponent $r = 150$ for the maximum increment of average simple shear $\Delta\bar{\gamma}_{12\,\mathrm{max}} = 10^{-3}$ and final macroscopic strain $\bar{\varepsilon}_{12} = 0.05$. Slip-system shear **a, d** $|\gamma^1|$, **b, e** $|\gamma^3|$ and **c, f** total accumulated slip γ for FE mesh **a–c** 40×40 and **d–f** 80×80

The results of computations made using the rate-independent (EM) algorithm show the formation of diagonal unidirectional bands in the middle of the sample as in Fig. 14. This character of the bands is observed during simulations with various FE mesh densities, in the analysed range from 40×40 to 160×160, as noted in Table 8.

Computations for rate-dependent algorithm (RD) have been performed using exponent $r = 150$ and macroscopic

shear rate $\dot{\bar{\varepsilon}}_{12} = 0.000943$ 1/s. The results show formation of crossed bidirectional bands in the middle of the sample, visible in Fig. 15. For the finer FE mesh 100×100, as well as for a mesh 160×160, the deformation band character in the center of the sample is somewhat different than for the EM results. The differences are not very significant and they are not observed for the coarser FE mesh, cf. Table 8.

Table 7 Summary of the CPU time and deformation character for the results of the macroscopically uniform simple shear in case $\omega = \pi/4$ using the incremental energy minimization algorithm (EM) and the rate-dependent algorithm (RD) with exponent $r = 150$

FE mesh	CPU time for $\Delta\bar{\gamma}_{12\,\text{max}} = 10^{-3}$	Deformation character
Incremental energy minimization algorithm (EM)		
40×40	6 m 5 s	Predominant diagonal unidirectional bands
80×80	36 m 46 s	Disordered fields of diagonal bands
160×160	3 h 43 m 8 s	Disordered fields of diagonal bands
Rate-dependent algorithm (RD), $r = 150$		
40×40	3 m 32 s	Predominant diagonal unidirectional bands
80×80	18 m 5 s	Regular fields of diagonal bands
160×160	2 h 9 m 46 s	Regular fields of diagonal bands

Calculations with the maximum increment of average simple shear $\Delta\bar{\gamma}_{12\,\text{max}} = 10^{-3}$ up to final strain $\bar{\varepsilon}_{12} = 0.05$, for both algorithms. Effect of FE mesh density on the formation of deformation bands
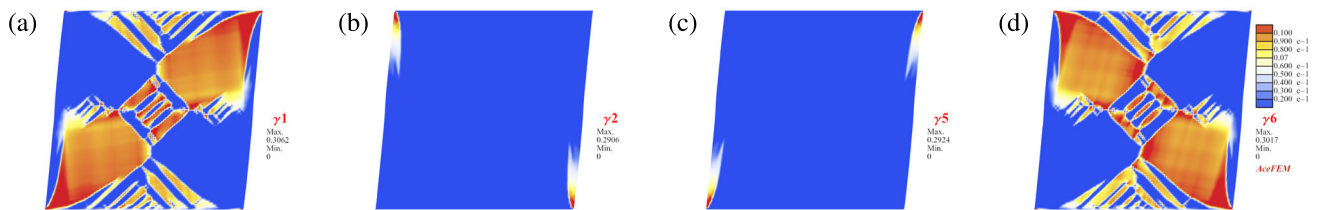
Fig. 14 Simple shear in case of orientation $\omega = \pi/4$ calculated by the incremental energy minimization algorithm (EM) for FE mesh 100×100 and maximum simple shear increment $\Delta\bar{\gamma}_{12\,\text{max}} = 10^{-3}$. Slip-systems shear **a** γ^1, **b** γ^2, **c** γ^5 and **d** γ^6 for final strain $\bar{\varepsilon}_{12} = 0.05$

Table 8 Summary of the CPU time and deformation character in the simple shear in case of orientation $\omega = \pi/4$

FE mesh	CPU time for $\Delta\bar{\gamma}_{12\,\text{max}} = 10^{-3}$	Deformation character
Incremental energy minimization algorithm (EM)		
40×40	4 m 27 s	Unidirectional diagonal bands in the middle
80×80	20 m 17 s	Unidirectional diagonal bands in the middle
100×100	43 m 11 s	Unidirectional diagonal bands in the middle
160×160	2 h 13 m 50 s	Unidirectional diagonal bands in the middle
Rate-dependent algorithm (RD), $r = 150$		
40×40	4 m 49 s	Unidirectional diagonal bands in the middle
80×80	29 m 17 s	Unidirectional diagonal bands in the middle
100×100	1 h 39 m 7 s	Bidirectional diagonal bands in the middle
160×160	5 h 10 m 27 s	Bidirectional diagonal bands in the middle

The effect of FE mesh density on the formation of deformation bands using the incremental energy minimization algorithm (EM) and the rate-dependent algorithm (RD) with exponent $r = 150$. Calculations with maximum simple shear increment $\Delta\bar{\gamma}_{12\,\text{max}} = 10^{-3}$ up to final strain $\bar{\varepsilon}_{12} = 0.05$, for both algorithms

Fig. 15 Simple shear in case of orientation $\omega = \pi/4$ calculated by the rate-dependent algorithm (RD) with exponent $r = 150$ for FE mesh 100×100 and maximum simple shear increment $\Delta\bar{\gamma}_{12\,\text{max}} = 10^{-3}$. Slip-systems shear **a** $|\gamma^1|$, **b** $|\gamma^2|$ and **c** $|\gamma^3|$ for final strain $\bar{\varepsilon}_{12} = 0.05$

For both algorithms (EM) and (RD), it can be noticed that as the mesh becomes denser, the number of bands increases, but this increase is not as large as in the case of plane-strain compression. In the case of bands formed during simple shear, they are oriented non-parallel to the FE grid and therefore their character is less correlated with the mesh density. The computation CPU time and the deformation character for various FE mesh densities are summarized in Table 8, for both element types. The EM algorithm is clearly less time consuming for finer FE meshes, e.g. 160×160.

6.5.3 Macroscopic simple shear with compression, $\omega = \pi/4$

In order to calculate a slightly more complex deformation process, simulation of simple shear in the horizontal direction (x_1) is realized with additional compression in vertical direction (x_2), while the bottom edge is clamped as previously. The geometry of the sample is the same as in the previous Sections. The final ratio of the horizontal displacement of top edge to sample height is equal to 0.1, now with the additional vertical displacement to height ratio of 0.05. This additional vertical compression resulted in a different character of the band.

The results of computations made using incremental energy minimization algorithm (EM) for different FE mesh density show formation of nearly vertical or horizontal bands

in the middle part of the sample, as shown in Fig. 16. If a coarser FE mesh is used, e.g. 40×40, the bands are nearly vertical, but if a finer mesh is used, e.g. 80×80, only nearly horizontal bands are obtained. The field of γ^1 is almost uniform except near the boundary, and therefore not shown.

Computations using the rate-dependent algorithm (RD) were performed as in the previous sections with exponent $r = 150$ and for the macroscopic shear rate $\dot{\bar{\varepsilon}}_{12} = 0.000943 \, 1/s$, cf. Fig. 17. The results of RD algorithm computations collected in Table 9 consistently show the formation of nearly vertical bands in the central part of the sample, regardless the values of exponent r or the density of the FEM mesh.

Similar character of vertical bands has been obtained for various values of the exponent $r = 50, 150, 300$ for FE mesh size 200×200, 150×150, 300×300, respectively, and maximum simple shear increment $\Delta\bar{\gamma}_{12\,\text{max}} = 10^{-3}$. Similar results were also obtained for larger values of exponent $r = 300, 800$ and 1000 calculated with FE mesh density 40×40 and maximum simple shear increment $\Delta\bar{\gamma}_{12\,\text{max}} = 10^{-4}$. The same character of the results was also found for a finer mesh e.g. 100×100, 200×200 and 300×300 with exponent $r = 150$ and different values of the maximum simple shear increment $\Delta\bar{\gamma}_{12\,\text{max}} = 10^{-4}$ and $\Delta\bar{\gamma}_{12\,\text{max}} = 10^{-2}$.

In this example it can be summarized that for finer meshes a different character of the resulting microstructures is obtained for the incremental energy minimization algorithm (EM) and for the rate-dependent algorithm (RD). The
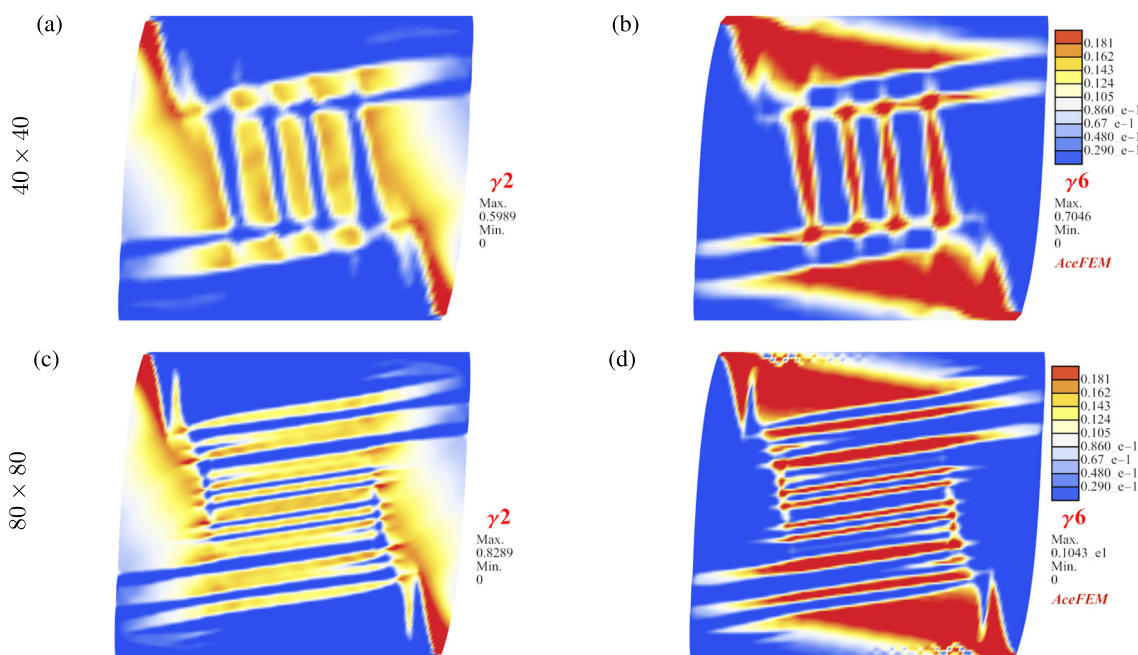

Fig. 16 Macroscopic simple shear with compression in case of $\omega = \pi/4$ calculated by the incremental energy minimization algorithm (EM) for maximum simple shear increment $\Delta\bar{\gamma}_{12\,\text{max}} = 10^{-3}$ up to final strain $\bar{\varepsilon}_{12} = 0.05$ and $\bar{\varepsilon}_{22} = -0.05$. Slip-systems shear **a**, **c** γ^2 and **b**, **c** γ^6 calculated for FE mesh **a**, **b** 40×40 and **c**, **d** 80×80
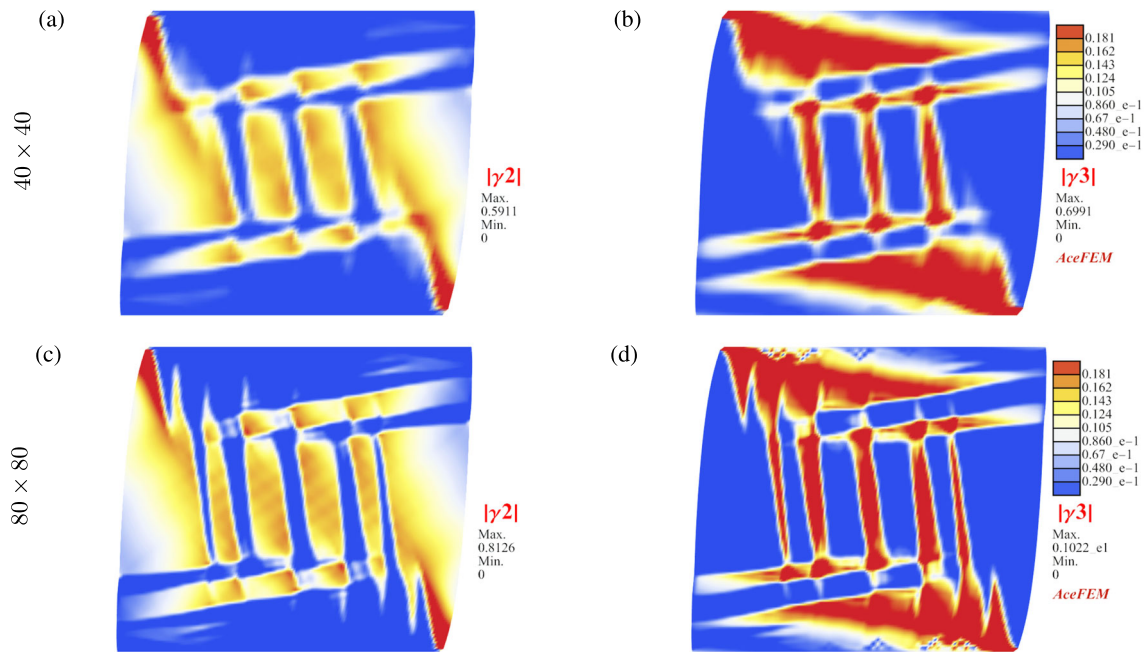
Fig. 17 Macroscopic simple shear with compression in case of $\omega = \pi/4$ calculated by the rate-dependent algorithm (RD) with exponent $r = 150$ to final strain $\bar{\varepsilon}_{12} = 0.05$ and $\bar{\varepsilon}_{22} = -0.05$ with maximum simple shear increment $\Delta\bar{\gamma}_{12\,\mathrm{max}} = 10^{-3}$. Slip-systems shear **a, c** $|\gamma^2|$ and **b, c** $|\gamma^3|$ calculated for FE mesh **a, b** 40×40 and **c, d** 80×80

Table 9 Summary of the CPU time and deformation character for the results of the simple shear with compression in case $\omega = \pi/4$ using incremental energy minimization algorithm (EM) and rate-dependent algorithm (RD) with exponent $r = 150$

FE mesh	CPU time for $\Delta\bar{\gamma}_{12\,\mathrm{max}} = 10^{-3}$	Deformation character
Incremental energy minimization algorithm (EM)		
40×40	5 m 58 s	Nearly vertical bands
80×80	29 m 42 s	Nearly horizontal bands
100×100	50 m 1 s	Nearly horizontal bands
160×160	2 h 42 m 7 s	Nearly horizontal bands
Rate-dependent algorithm (RD), $r = 150$		
40×40	6 m 59 s	Nearly vertical bands
80×80	53 m 4 s	Nearly vertical bands
100×100	1 h 46 m 40 s	Nearly vertical bands
150×150	7 h 36 m 55 s	Nearly vertical bands
160×160	9 h 41 m 44 s	Nearly vertical bands

Calculations with maximum simple shear increment $\Delta\bar{\gamma}_{12\,\mathrm{max}} = 10^{-3}$ up to final strain $\bar{\varepsilon}_{12} = 0.05$ and $\bar{\varepsilon}_{22} = -0.05$, for both algorithms. Effect of FEM mesh density on the formation of deformation bands

latter gives nearly vertical deformation bands independently of the FE mesh density, while the EM algorithm gives nearly horizontal deformation bands for finer meshes and vertical bands only for a sparse FE mesh, cf. Table 9.

6.5.4 Computations with constant deformation step for plane-strain compression in case $\omega = \pi/4$

Finally, in order to compare the calculation CPU time for the algorithms EM and RD without using the FE adaptive time step control, simulations were performed with a constant

deformation step from the range $\Delta\bar{\varepsilon}_{22} = 10^{-6} \div 10^{-2}$. For both algorithms, plane-strain compression was performed in case of orientation $\omega = \pi/4$. The dimensions, geometry and the boundary conditions of the sample were the same as in Sect. 6.3, the mesh density was 20×20. For compression in this orientation, a single slip-system γ^5 is active in the entire sample and the deformation is practically uniform, with no visible bands. In the case of the rate-dependent algorithm (RD) with $\Delta\bar{\varepsilon}_{22} = 10^{-5}$, calculations were performed for several different values of exponent $r = 10, 20, 50, 100$ as shown in Table 10. For the smaller step size, CPU times for

Table 10 Summary of the CPU time for uniform plane-strain compression in case $\omega = \pi/4$ with constant deformation step using the incremental energy minimization algorithm (EM) and the rate-dependent algorithm (RD)

$\Delta\bar{\varepsilon}_{22}$	CPU time Incremental energy minimization (EM)	$\Delta\bar{\varepsilon}_{22}$	CPU time Rate-dependent algorithm (RD)
10^{-6}	3 h 50 m 48 s	10^{-6}	4 h 26 m 18 s for $r = 100$
10^{-5}	13 m 46 s	10^{-5}	19 m 35 s average for $r = 10, 20, 50, 100$
10^{-4}	1 m 21 s	10^{-4}	19 m 28 s for $r = 10$
10^{-3}	11 s	10^{-3}	No convergence for $r \geq 10$
10^{-2}	2 s	10^{-2}	No convergence for $r \geq 10$

Computations for FE mesh density 20×20 and final compressive strain $\bar{\varepsilon}_{22} = 0.1$

both algorithms are comparable, with a slight advantage of the EM algorithm. However, for the largest constant deformation steps $\Delta\bar{\varepsilon}_{22} = 10^{-3}$ and 10^{-2}, the RD algorithm caused a convergence issue even for small values of exponent $r \geq 10$, while the EM algorithm worked effectively.

7 Conclusions

Spontaneous formation of deformation bands has been observed in the plane-strain FE simulations of single crystal plasticity at small strain. This has been attributed to the yield-vertex effect in the case when the latent-hardening of slip systems is higher than the self-hardening. The new observation is that this source of deformation banding was activated only due to numerical inaccuracies in the FE simulations, without introducing artificial imperfections or any mechanism favouring deformation banding in the numerical code. A characteristic feature of the deformation band pattern obtained for various plane-strain examples was the appearance of regions with two families of bands with alternating activity of a single (effective) slip system. Such deformation banding, activated by numerical inaccuracies in the FE simulations, can be interpreted as a symptom of the inherent instability of uniform deformation of the material model used, which is consistent with the experimentally observed mechanism of plastic deformation in metal single crystals.

In the examined case of macroscopically uniform plane-strain compression, the banding pattern corresponds to the lower global deformation work than uniform straining and can therefore be assigned a physical significance. The bands appeared spontaneously, also for the rate-dependent material model. However, in general, the generated band pattern is not unique, so the need for global incremental energy minimization (in the potential case) has not been completely eliminated.

It has been found that numerical inaccuracies are sufficient to trigger the banding instability when the inverse of the strain-rate sensitivity exponent m is not less than 150 (or infinity in the rate-independent limit). Moreover, roughly, when the time step corresponds to macroscopic strain increment 10^{-3} or lower, and the mesh resolution is sufficiently fine (e.g. 30×30) to detect bands that are not aligned with the grid lines.

These numerical conditions for activation of deformation banding should be considered as indicative only, as they have been identified for the specific plane-strain examples and may depend on many other factors, e.g., the use of biquadratic shape functions with (3×3) Gauss quadrature points or the algorithm used. Nevertheless, they help to understand why the banding pattern has not been widely observed in FE simulations before.

An important general observation is that the overall response of the crystal, represented by the average stress versus average strain curve in plane strain compression, is insensitive to mesh density. Thus, in contrast to simulations of a single shear band triggered by material softening, the mesh-dependence of the width of individual deformation bands is not so crucial here.

For a rate-independent single crystal, an algorithm for selection of active slip-systems at the Gauss point level, based on non-convex minimization of incremental work using the trust region approach and the augmented Lagrangian method, has been developed and effectively used in the FE calculations. The implemented algorithm may be a good alternative to other algorithms encountered in the literature.

References

1. Anand L, Kalidindi SR (1994) The process of shear band formation in plane strain compression of FCC metals: effects of crystallographic texture. Mech Mater 17(2–3):223–243

2. Anand L, Kothari M (1996) A computational procedure for rate-independent crystal plasticity. J Mech Phys Solids 44(4):525–558

3. Anderson E, Bai Z, Bischof C et al (1999) LAPACK users' guide, 3rd edn. Society for Industrial and Applied Mathematics, Philadelphia

4. Arora R, Acharya A (2020) Dislocation pattern formation in finite deformation crystal plasticity. Int J Sol Struct 184:114–135. Physics and Mechanics of Random Structures: From Morphology to Material Properties

5. Barrett CS, Levenson LH (1939) Structure of iron after drawing, swaging and elongation in tension. Trans AIME 135:327–352

6. Basson F, Driver JH (2000) Deformation banding mechanisms during plane strain compression of cube-oriented f.c.c. crystals. Acta Mater 48:2101–2115

7. Bay B, Hansen N, Kuhlmann-Wilsdorf D (1989) Deformation structures in lightly rolled pure aluminium. Mater Sci Eng A 113:385–397

8. Bay B, Hansen N, Hughes DA et al (1992) Evolution of f.c.c. deformation structures in polyslip. Acta Metall Mater 40(2):205–219

9. Bertsekas DP (1996) Constrained optimization and Lagrange multiplier methods, 2nd edn. Athena Scientific, Belmont

10. Bronkhorst CA, Kalidindi SR, Anand L (1992) Polycrystalline plasticity and the evolution of crystallographic texture in FCC metals. Philos Trans R Soc Lond A 341(1662):443–477

11. Brown SB, Kim KH, Anand L (1989) An internal variable constitutive model for hot working of metals. Int J Plasticity 5(2):95–130

12. Butler GC, Stock SR, McGinty RD et al (2002) X-ray microbeam Laue pattern studies of the spreading of orientation in OFHC copper at large strains. J Eng Mater Technol 124(1):48–54

13. Cai L, Jebahi M, Abed-Meraim F (2021) Strain localization modes within single crystals using finite deformation strain gradient crystal plasticity. Cryst 11(10):1235

14. Carstensen C, Conti S, Orlando A (2008) Mixed analytical-numerical relaxation in finite single-slip crystal plasticity. Continuum Mech Thermodyn 20(5):275–301

15. Chin GY, Wonsiewicz BC (1969) Deformation banding and stability of (100)-(111) fiber textures of fcc metals. Trans Metall Soc AIME 245(4):871

16. Conn AR, Gould NI, Toint PL (2000) Trust region methods. SIAM, Philadelphia

17. Conti S, Theil F (2005) Single-slip elastoplastic microstructures. Arch Ration Mech Anal 178(1):125–148

18. Cuitiño AM, Ortiz M (1993) Computational modelling of single crystals. Model Simul Mater Sci Eng 1(3):225–263

19. Dequiedt J, Denoual C, Madec R (2015) Heterogeneous deformation in ductile FCC single crystals in biaxial stretching: the influence of slip system interactions. J Mech Phys Solids 83:301–318

20. Dittmann J, Wulfinghoff S (2023) Efficient numerical strategies for an implicit volume fraction transfer scheme for single crystal plasticity including twinning and secondary plasticity on the example of magnesium. Int J Numer Methods Eng 124(21):4718–4739

21. Dmitrieva O, Dondl PW, Müller S et al (2009) Lamination microstructure in shear deformed copper single crystals. Acta Mater 57:3439–3449

22. Hackl K, Hoppe U (2003) On the calculation of microstructures for inelastic materials using relaxed energies. In: Miehe C (ed) IUTAM symposium on computational mechanics of solid materials at large strains, solid mechanics and its applications, vol 108. Springer, Dordrecht, pp 77–86

23. Hansen BL, Bronkhorst CA, Ortiz M (2010) Dislocation subgrain structures and modeling the plastic hardening of metallic single crystals. Model Simul Mater Sci Eng 18:055001

24. Harewood F, McHugh P (2006) Investigation of finite element mesh independence in rate dependent materials. Comput Mater Sci 37(4):442–453

25. Hill R, Rice JR (1972) Constitutive analysis of elastic-plastic crystals at arbitrary strain. J Mech Phys Solids 20:401–413

26. Homayonifar M, Mosler J (2012) Efficient modeling of microstructure evolution in magnesium by energy minimization. Int J Plasticity 28(1):1–20

27. Honeycombe RWK (1951) Inhomogeneities in the plastic deformation of metal crystals. 2. X-ray and optical micrography of aluminium. J Inst Metals 80:49–56

28. Huang X, Hansen N (1997) Grain orientation dependence of micorstructure in aluminium deformed in tension. Scr Mater 37(1):1–7

29. Huang X, Winther G (2007) Dislocation structures. Part I. Grain orientation dependence. Philos Mag 87(33):5189–5214

30. Huang X, Chen Y, Wang J et al (2024) High-resolution reconstruction-based investigation of multi-scale lamellar microstructures by coupled crystal plasticity and in-situ experiment. Scr Mater 241:115896

31. Huang Y (1991) A User-material Subroutine Incorporating Single Crystal Plasticity in the ABAQUS Finite Element Program. Division of Applied Sciences, Harvard University, Cambridge, MA, report Mech-178

32. Hughes DA, Liu Q, Chrzan DC et al (1997) Scaling of microstructural parameters: misorientations of deformation induced boundaries. Acta Mater 45(1):105–112

33. Hutchinson JW (1976) Bounds and self-consistent estimates for creep of polycrystalline materials. Proc R Soc Lond A 348(1652):101–127

34. Jebahi M, Cai L, Abed-Meraim F (2020) Strain gradient crystal plasticity model based on generalized non-quadratic defect energy and uncoupled dissipation. Int J Plasticity 126:102617

35. Jeong J, Voyiadjis GZ (2022) A physics-based crystal plasticity model for the prediction of the dislocation densities in micropillar compression. J Mech Phys Solids 167:105006

36. Klusemann B, Kochmann DM (2014) Microstructural pattern formation in finite-deformation single-slip crystal plasticity under cyclic loading: Relaxation vs. gradient plasticity. Comput Methods Appl Mech Eng 278:765–793

37. Klusemann B, Yalçinkaya T (2013) Plastic deformation induced microstructure evolution through gradient enhanced crystal plasticity based on a non-convex Helmholtz energy. Int J Plasticity 48:168–188

38. Kochmann DM, Hackl K (2011) The evolution of laminates in finite crystal plasticity: a variational approach. Continuum Mech Thermodyn 23:63–85

39. Kochmann J, Wulfinghoff S, Ehle L et al (2018) Efficient and accurate two-scale FE-FFT-based prediction of the effective material behavior of elasto-viscoplastic polycrystals. Comput Mech 61(6):751–764

40. Kocks UF (1970) The relation between polycrystal deformation and single-crystal deformation. Metall Trans 1:1121–1142

41. Korelc J (2009) Automation of primal and sensitivity analysis of transient coupled problems. Comput Mech 44:631–649

42. Korelc J, Wriggers P (2016) Automation of finite element methods. Springer, Cham

43. Kratochvíl J, Kružík M (2016) Statistically motivated model of mechanisms controlling evolution of deformation band substructure. Int J Plasticity 81:196–208

44. Kratochvíl J, Kružík M, Sedláček R (2010) Crystal plasticity model of shear and kink bands-energetic approach. Philos Mag 90(27–28):3729–3742

45. Kratochvíl J, Kružík M, Sedláček R (2010) Instability origin of subgrain formation in plastically deformed materials. Int J Eng Sci 48:1401–1412

46. Kuhlmann-Wilsdorf D, Kulkarni SS, Moore JT et al (1999) Deformation bands, the LEDS theory, and their importance in texture development: Part I. Previous evidence and new observations. Metall Mater Trans A 30:2491–2501

47. Kumar S, Vidyasagar A, Kochmann DM (2020) An assessment of numerical techniques to find energy-minimizing microstructures associated with nonconvex potentials. Int J Numer Methods Eng 121(7):1595–1628

48. Kuroda M (2016) A strain-gradient plasticity theory with a corner-like effect: a thermodynamics-based extension. Int J Fract 200(1–2):115–125

49. Kuroda M, Needleman A (2019) Nonuniform and localized deformation in single crystals under dynamic tensile loading. J Mech Phys Solids 125:347–359

50. Kysar J, Saito Y, Oztop M et al (2010) Experimental lower bounds on geometrically necessary dislocation density. Int J Plasticity 26(8):1097–1123. Special Issue In Honor of Lallit Anand

51. Lancioni G, Yalçinkaya T, Cocks A (2015) Energy-based non-local plasticity models for deformation patterning, localization and fracture. Proc R Soc A 471:20150275

52. Lebensohn R, Tomé C (1993) A self-consistent anisotropic approach for the simulation of plastic deformation and texture development of polycrystals: Application to zirconium alloys. Acta Metall Mater 41(9):2611–2624

53. Lee CS, Duggan BJ (1993) Deformation banding and copper-type rolling textures. Acta Metall Mater 41:2691–2699

54. Lee CS, Duggan BJ, Smallman RE (1993) A theory of deformation banding in cold rolling. Acta Metall Mater 41(8):2265–2270

55. Lewandowski M, Stupkiewicz S (2018) Size effects in wedge indentation predicted by a gradient-enhanced crystal-plasticity model. Int J Plasticity 109:54–78

56. Luan Q, Xing H, Zhang J et al (2020) Experimental and crystal plasticity study on deformation bands in single crystal and multicrystal pure aluminium. Acta Mater 183:78–92

57. Lynggaard J, Nielsen K, Niordson C (2019) Finite strain analysis of size effects in wedge indentation into a Face-Centered Cubic (FCC) single crystal. Eur J Mech A/Solids 76:193–207

58. Ma A, Roters F, Raabe D (2006) A dislocation density based constitutive model for crystal plasticity FEM including geometrically necessary dislocations. Acta Mater 54(8):2169–2179

59. Ma A, Roters F, Raabe D (2006) On the consideration of interactions between dislocations and grain boundaries in crystal plasticity finite element modeling - Theory, experiments, and simulations. Acta Mater 54(8):2181–2194

60. Mánik T, Asadkandi H, Holmedal B (2022) A robust algorithm for rate-independent crystal plasticity. Comput Methods Appl Mech Eng 393:114831

61. Marano A, Gélébart L, Forest S (2019) Intragranular localization induced by softening crystal plasticity: analysis of slip and kink bands localization modes from high resolution FFT-simulations results. Acta Mater 175:262–275

62. Miehe C, Schröder J (2001) A comparative study of stress update algorithms for rate-independent and rate-dependent crystal plasticity. Int J Numer Methods Eng 50(2):273–298

63. Miehe C, Lambrecht M, Gürses E (2004) Analysis of material instabilities in inelastic solids by incremental energy minimization and relaxation methods: evolving deformation microstructures in finite plasticity. J Mech Phys Solids 52:2725–2769

64. Moré JJ, Sorensen D (1983) Computing a trust region step. SIAM J Sci Stat Comput 4(3):553–572

65. Niehüser A, Mosler J (2023) Numerically efficient and robust interior-point algorithm for finite strain rate-independent crystal plasticity. Comput Methods Appl Mech Eng 416:116392

66. Nocedal J, Wright SJ (2006) Numerical optimization. Springer series in operation research and financial engineering, 2nd edn. Springer, New York

67. Ortiz M, Repetto EA (1999) Nonconvex energy minimization and dislocation structures in ductile single crystals. J Mech Phys Solids 47:286–351

68. Ortiz M, Repetto EA, Stainier L (2000) A theory of subgrain dislocation structures. J Mech Phys Solids 48:2077–2114

69. Peirce D, Asaro RJ, Needleman A (1982) An analysis of nonuniform and localized deformation in ductile single crystals. Acta Metall 30(6):1087–1119

70. Peirce D, Asaro RJ, Needleman A (1983) Material rate dependence and localized deformation in crystalline solids. Acta Metall 31(12):1951–1976

71. Petryk H (1992) Material instability and strain-rate discontinuities in incrementally nonlinear continua. J Mech Phys Solids 40(6):1227–1250

72. Petryk H (1993) Stability and constitutive inequalities in plasticity. In: Muschik W (ed) Non-equilibrium thermodynamics with application to solids, CISM courses and lectures, vol 336. Springer, Wien, pp 259–329

73. Petryk H (2000) General conditions for uniqueness in materials with multiple mechanisms of inelastic deformation. J Mech Phys Solids 48:367–396

74. Petryk H (2003) Incremental energy minimization in dissipative solids. C R Mecanique 331:469–474

75. Petryk H, Kursa M (2013) The energy criterion for deformation banding in ductile single crystals. J Mech Phys Solids 61(8):1854–1875

76. Petryk H, Kursa M (2015) Incremental work minimization algorithm for rate-independent plasticity of single crystals. Int J Numer Methods Eng 104(3):157–184

77. Petryk H, Kursa M (2022) Crystal plasticity algorithm based on the quasi-extremal energy principle. Int J Numer Methods Eng 123(14):3285–3316

78. Petryk H, Thermann K (1995) On plastic strain localisation in the non-elliptic range under plane stress. In: Owen DRJ, Onate E (eds) Computational plasticity: fundamentals and applications. Pineridge Press, Swansea, pp 647–658

79. Petryk H, Thermann K (2000) Post-critical deformation pattern in plane strain plastic flow with yield-surface vertex effect. Int J Mech Sci 42:2133–2146

80. Petryk H, Thermann K (2002) Post-critical plastic deformation in incrementally nonlinear materials. J Mech Phys Solids 50:925–954

81. Phalke V, Forest S, Chang HJ et al (2022) Adiabatic shear banding in FCC metallic single and poly-crystals using a micromorphic crystal plasticity approach. Mech Mater 169:104288

82. Prüger S, Kiefer B (2020) A comparative study of integration algorithms for finite single crystal (visco-)plasticity. Int J Mech Sci 180:105740

83. Rice JR (1971) Inelastic constitutive relations for solids: an internal-variable theroy and its application to metal plasticity. J Mech Phys Solids 19:433–455

84. Rice JR (1987) Tensile crack tip fields in elastic-ideally plastic crystals. Mech Mater 6(4):317–335

85. Russo R, Phalke V, Croizet D et al (2022) Regularization of shear banding and prediction of size effects in manufacturing operations: a micromorphic plasticity explicit scheme. Int J Mater Form 15:21

86. Scherer JM, Phalke V, Besson J et al (2020) Lagrange multiplier based vs micromorphic gradient-enhanced rate-(in)dependent crystal plasticity modelling and simulation. Comput Methods Appl Mech Eng 372:113426

87. Scheunemann L, Nigro P, Schröder J et al (2020) A novel algorithm for rate independent small strain crystal plasticity based on the infeasible primal-dual interior point method. Int J Plasticity 124:1–19

88. Simmons G, Wang H (1971) Single crystal elastic constants and calculated aggregate properties: a handbook, 2nd edn. M.I.T Press, Cambridge

89. Sorensen D (1982) Newton's method with a model trust region modification. SIAM J Numer Anal 19(2):409–426

90. Taylor GI (1938) Analysis of plastic strain in a cubic crystal. In: Lessels JM (ed) Stephen Timoshenko 60th Anniversary Volume. Macmillan, New York, pp 218–224

91. Vermeij T, Wijnen J, Peerlings R et al (2024) A quasi-2D integrated experimental-numerical approach to high-fidelity mechanical analysis of metallic microstructures. Acta Mater 264:119551

92. Vidyasagar A, Tutcuoglu AD, Kochmann DM (2018) Deformation patterning in finite-strain crystal plasticity by spectral homogenization with application to magnesium. Comput Methods Appl Mech Eng 335:584–609

93. Voyiadjis G, Jeong J, Kysar J (2021) Grain size dependence of polycrystalline plasticity modeling in cylindrical indentation. Comput Mech 68:499–543

94. Wang D, Diehl M, Roters F et al (2018) On the role of the collinear dislocation interaction in deformation patterning and laminate formation in single crystal plasticity. Mech Mater 125:70–79

95. Wert JA, Huang X, Inoko F (2003) Deformation bands in a [110] aluminium single crystal strained in tension. Proc R Soc Lond A 459:85–108

96. Wijnen J, Peerlings R, Hoefnagels J et al (2021) A discrete slip plane model for simulating heterogeneous plastic deformation in single crystals. Int J Sol Struct 228:111094

97. Yalçinkaya T, Brekelmans W, Geers M (2012) Non-convex rate dependent strain gradient crystal plasticity and deformation patterning. Int J Sol Struct 49:2625–2636

98. Zhang M, Nguyen K, Segurado J et al (2021) A multiplicative finite strain crystal plasticity formulation based on additive elastic corrector rates: theory and numerical implementation. Int J Plasticity 137:102899